Fragility of reaction-diffusion models with respect to competing advective processes

Oleg Kogan*
Laboratory of Atomic and Solid State Physics, Cornell University, Ithaca, New York 14853, USA

Kevin O'Keeffe
Center for Applied Mathematics, Cornell University, Ithaca, New York 14853, USA

Christopher R. Myers
Laboratory of Atomic and Solid State Physics, and Institute of Biotechnology, Cornell University, Ithaca, New York 14853, USA
(Received 8 April 2016; revised manuscript received 26 May 2017; published 29 August 2017)

We study the coupling of a Fisher-Kolmogorov-Petrovsky-Piskunov (FKPP) equation to a separate, advection-only transport process. We find that an infinitesimal coupling can cause a finite change in the speed and shape of the reaction front, indicating the fragility of the FKPP model with respect to such a perturbation. The front dynamics can be mapped to an effective FKPP equation only at sufficiently fast diffusion or large coupling strength. We also discover conditions when the front width diverges and when its speed is insensitive to the coupling. At zero diffusion in our mean-field description, the downwind front speed goes to a finite value as the coupling goes to zero.

DOI: 10.1103/PhysRevE.96.022220

I. INTRODUCTION

The Fisher-Kolmogorov-Petrovsky-Piskunov (FKPP) equation, originally introduced to describe the population dynamics of the spread of advantageous genes [1] has found applications in a very wide range of contexts that include ecology [2], epidemiology [2], population biology [2,3], chemical kinetics [4], extreme-value statistics [5], disordered systems [6], and even high-energy physics [7]. It describes reaction-diffusion processes involving saturation-limited growth and diffusion, and admits front-like solutions—known as Fisher waves—that invade a linearly unstable state.

Often, reaction-diffusion processes are coupled to an additional advective process. In some models, an advective term is added to the FKPP equation, such that reactions, advection, and diffusion occur simultaneously. This can give rise to rich phenomenology—for instance, when disorder is involved [3,8], or when reactions release heat [9], causing the coupling between the concentration of reacting species and the advective flow field. In other instances, however, advection takes place in a separate competing transport channel, often associated with a flow over a substrate on which reaction-diffusion processes take place. Examples include heterogeneous catalysis on surfaces under flow [10,11], population ecology in streams [12,13], microbial population dynamics in the digestive tract [14,15], and the long-range aerial spread of fungal plant pathogens—the original motivation for this work [16–18]. In all of these examples, there is a reaction-diffusion region, such as a catalytic substrate or a biological growth layer, and an advection region alongside it—with adsorption and desorption taking material on and off the growth layer—as depicted schematically in Fig. 1. In this paper, we study this specific scenario whereby advection competes with a separate reaction-diffusion process.

As we demonstrate, the presence of a competing transport mechanism causes the results of the FKPP model to be fragile if diffusion is slow-enough—giving a finite change in results due to an infinitesimal coupling. We thus identify a perturbation that causes predictions of a reaction-diffusion model to fail. At fast-enough diffusion or large-enough desorption rate, it is possible to map the coupled process to an effective FKPP equation with an advective term and suitably adjusted parameters.

II. THEORETICAL FRAMEWORK

Let $\rho(\mathbf{x},t)$ and $\sigma(\mathbf{x},t)$ denote the number density in the advective and reactive layers, respectively. The advective layer has an imposed velocity field $\mathbf{v}$. Then, ignoring finite-number fluctuations (mean-field description), the spatiotemporal dynamics of $\rho(\mathbf{x},t)$ and $\sigma(\mathbf{x},t)$ will evolve from initial conditions $\rho(\mathbf{x},0) > 0$ and $\sigma(\mathbf{x},0) > 0$, according to

$$\frac{\partial \rho}{\partial t} = -\nabla \cdot (\mathbf{v}\rho) + \alpha\sigma - \beta\rho, \tag{1}$$

$$\frac{\partial \sigma}{\partial t} = \delta f(\sigma) - \alpha\sigma + \beta\rho + D\nabla^2\sigma. \tag{2}$$

We discuss the validity of this mean-field description below. In contrast to the FKPP model with an advective term, here any one particle either reacts and diffuses or advects within

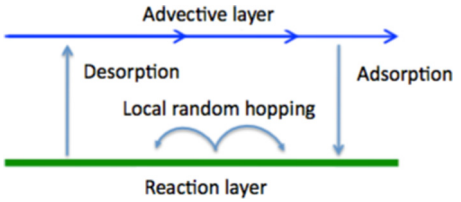

FIG. 1. Reaction-diffusion process coupled to advection.

*obk5@cornell.edu

 ©2017 American Physical Society

a small time interval Δt. Here, $\alpha > 0$ and $\beta > 0$ are rates of mass transfer between the two layers, and δ is a characteristic reaction rate—all with dimensions [$time^{-1}$]. In this paper, we focus on one reactant, so Eqs. (1) and (2) are specific to growth-type reactions, and the reaction layer will be called the growth layer (GL). The function $f(\sigma)$ is a dimensionless growth rate. D is a diffusion constant on the GL.

We focus in this paper on one dimension with a constant advective velocity v_0. We assume $f(\sigma)$ is a concave and smooth function that admits one unstable state at $\sigma = 0$, where $df/d\sigma = 1$ and $f = 0$, and a stable state at $\sigma = \sigma_{\max}$. In some cases we will use a logistic model as a concrete example: $f(\sigma) = \sigma(1 - \sigma/\sigma_{\max})$. Since our main objective is to study the role of coupling of the FKPP equation to an independent advective process, this class of $f(\sigma)$ is a natural choice, because it is also usually employed in the FKPP equation.

A natural length scale is v_0/δ—the distance traveled by the advective layer (AL) per characteristic growth time. Rescaling x by v_0/δ, t by $1/\delta$, and σ, ρ by $\sigma_{\max}$, we are left with three parameters: $a \equiv \alpha/\delta$, $b \equiv \beta/\delta$, and $\mathcal{D} = (\delta D/v_0^2)$, with speed and growth rate both becoming 1 in these units (i.e., speed is now in units of v_0); we will continue to use the letters ρ, σ, x, t, and f. Unless otherwise specified, calculations will be done with Eqs. (1) and (2) nondimensionalized in this way.

It will prove useful to first study the $\mathcal{D} = 0$ case and then consider the effect of diffusion.

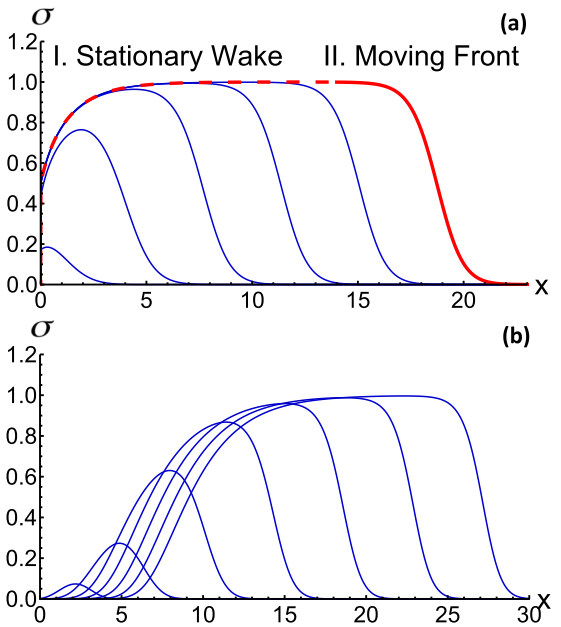

FIG. 2. Evolution of the GL profile from a δ-function IC with a logistic growth model and no diffusion. (a) $a = 0.5$, $b = 1$ at $t = 5$, 10, 15, 20, 25, and 30. (b) $a = 2$, $b = 1$, same ts. In both cases, the IC launches uniformly translating fronts (UTF). Early transients are not shown.

III. ZERO DIFFUSION

We first describe the qualitative picture. Consider a patch of GL around position x_0. It produces new mass and loses mass to the AL at rate a. Once there, the mass is swept along at speed 1 by the advection. All the while, mass is continuously shed onto the parts of the GL at $x > x_0$ with rate b. The returned mass resumes growth at these new locations of the GL, while at the same time continuing redesorption back onto the AL, and so on.

In the zero-diffusion case, without the deposition of new mass from the AL, the dynamics on the GL unfolds independently at each x following an initial condition (IC). The advective layer effectively couples different locations of the growth layer. The dynamics of the GL at each x is driven by the AL, which itself is a result of accumulation of the upstream GL density. The state $\sigma = 0$, $\rho = 0$ is linearly unstable to perturbations over a low wave vector range (see Appendix B). The nonlinearity limits the growth. Thus, an IC that decays to 0 as $x \to \pm\infty$ leads to traveling fronts.

Typical $\sigma(x)$ profiles are depicted in Fig. 2; $\rho(x)$ is qualitatively similar. Here, the advective velocity is directed rightward. We will only consider ICs with a finite support; its left edge set at $x = 0$. Figure 2 depicts profiles at various times, evolving from a δ-function IC at $x = 0$, but qualitatively similar picture holds for all ICs with a finite support. Depending on parameters, the profiles have one or two moving fronts.

If the desorption rate is slower than the growth rate ($a < 1$), there is an asymptotically stationary part of the profile left behind a single front propagating in the advective direction. It is depicted as a thick dashed part of the profile in Fig. 2(a) (section "I. Stationary Wake"), while the moving front is depicted as the thick solid curve (section "II. Moving Front"). Stationary profiles are discussed in Appendix D. When $a\sigma > f(\sigma)$ for any $0 < \sigma < 1$—regardless of the convexity of $f(\sigma)$—there are two moving fronts—one leading ("downwind") and one trailing ("upwind"), with a plateau in between—Fig. 2(b). Note that in the absence of diffusion and for ICs with a finite support, a front cannot propagate backwards, since there is no mechanism that allows movement against the advective direction. On the other hand, in the presence of diffusion, upwind front can propagate either backwards, forwards, or stall—we explore this in Sec. IV. Also, because the $\mathcal{D} = 0$ model is hyperbolic, ICs with initially finite support will always lead to density profiles that also have a finite support.

We now study the long-time behavior of moving fronts; transients will not be addressed. We define the front speed s as the speed of $x(t)$ that satisfies $\rho(x,t) = c_0$, with $c_0 > 0$, i.e., the speed at some reference density c_0. In many systems, s is determined by the growth of the leading edge of the profile where the linear approximation is valid [19]. Such fronts are called "pulled." We proceed with this assumption—it will be validated by the comparison with numerical solutions of Eqs. (1) and (2). So, we let $f(\sigma) \to \sigma$ in Eqs. (1) and (2), solve the resulting equation, and compute s. Due to the linearity of the equation, the resulting speed is independent of the value of c_0. The speed defined by $\sigma(x,t) = c_0$ is identical, since ρ and σ are both governed by the same dispersion relation, and the same pair of ICs.

For the physically important IC $\sigma_0(x) = M\delta(x)$ and $\rho_0(x) = 0$ (profiles evolving from this IC are denoted by $*$), we can obtain a long-time asymptotically exact solution to the

linearized equations:

$$\rho^*(x,t) = \begin{cases} aMe^{-\kappa(x-wt)} I_0(2\sqrt{ab}\sqrt{x(t-x)}), & 0 < x < t, \\ 0, & \text{otherwise}, \end{cases}$$
$$\kappa = 1 - a + b, \quad w = (1-a)/(1-a+b). \tag{3}$$

To obtain this, we found the dispersion relation of the linearized equations, computed the Fourier integral on a contour in the complex plane around a branch cut, and approximated the result by the modified Bessel function I_0 for $t > (ab)^{-1/2}$. Details and $\sigma^*(x,t)$ are in Appendix B. Using $I_0(z) \sim \frac{e^z}{\sqrt{2\pi z}}$ for large z, the front speeds are given by

$$s_\pm^* = \left(1 + \frac{b}{(1 \pm \sqrt{a})^2}\right)^{-1} \tag{4}$$

for $a \geqslant 1$. The $+$ and $-$ represent the downwind and upwind profiles, respectively. For $a \leqslant 1$, $s_-^* = 0$ (upwind front does not move with zero diffusion and $a \leqslant 1$), but Eq. (4) applies for s_+^*. Note: when $a = 0$, Eq. (4) does not apply, since $\rho^* = 0$ and $\sigma^* = 0$ for $x > 0$; when only $b = 0$, then only $\sigma^* = 0$ for $x > 0$ (Appendix B).

The characteristic front width is $1/|\lambda_\pm^*|$, where

$$\lambda_\pm^* = \frac{1 + a + b \pm 2\sqrt{a}}{1 \pm \sqrt{a}} \tag{5}$$

is the negative of the spatial growth rate of tails of the solution in Eq. (3) at $c_0 \ll 1$. Defined this way, the decaying downwind front has $\lambda_+^* > 0$, while the growing upwind front has $\lambda_-^* < 0$ for $a > 1$. For $a < 1$, the upwind front is not moving and λ_-^* becomes meaningless. The value of c_0 may affect the time to attain $s_\pm^*$ and $\lambda_\pm^*$, but not their values. Equations (4) and (5) can also be obtained by the saddle-point method (Appendix C), which only requires that the Fourier Transform of the IC does not contain poles. Therefore, our results for $\lambda_\pm^*$ and $s_\pm^*$ apply to any IC with a finite support.

The finite speed of the downwind front as couplings approach (but $\neq$) zero, see Fig. 3, is the key prediction of the mean-field theory when $\mathcal{D} = 0$. The match with numerical calculations [20] supports the validity of the pulled front assumption.

The prediction that $s_+^* \to \text{const} \neq 0$ as $a \to 0$ at fixed b is most surprising. A parcel of mass that enters the AL—for however brief a period of time—will travel with speed 1 downstream, and because this is a continuum theory, there will always be mass present in the AL. So, the seeding process advances with speed 1. The speed of the front is defined at a constant density contour, so in general it is less than 1. As $a \to 0$, the AL density $\rho \to 0$, but the speed remains finite.

At sufficiently small a, the particle density in the AL becomes so small that the continuum theory breaks down. Our predictions will not apply when the number of particles within a region of AL of the width of the feature size, i.e., front width, becomes $\sim O(1)$. In physical units, the maximum number of particles in the AL within Δx is $(a/b)\sigma_{\max}\Delta x$. Therefore, mean-field theory predictions will hold as long as $\frac{a}{b} \gg \frac{\delta\lambda(a,b)}{\sigma_{\max} v_0}$, where $\sigma_{\max}$ is the carrying capacity on the GL per unit length. Otherwise, a stochastic treatment is needed. This threshold can be extremely small due to large $\sigma_{\max}$. For example, in applications to fungal pathogen transport by wind, we estimate in Appendix F that $\frac{\delta\lambda(a,b)}{\sigma_{\max} v_0} \sim O(10^{-14})$, and we argue there that realistic atmospheric mixing ensures that a/b is indeed much greater.

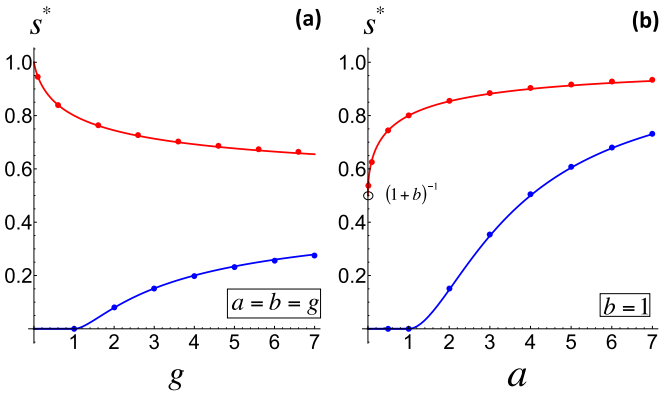

FIG. 3. (a) Front speeds vs. the interlayer coupling $a = b = g$ for a δ-function IC in the GL. Upper curve (red)—downwind front speed s_+^*, lower curve (blue)—upwind front speed s_-^*. For $g < 1$ there is a stationary profile behind the downwind front. Solid dots are from the numerical solution of Eqs. (1) and (2). (b) Front speeds vs. a at $b = 1$. Now $s_+^* \to (1+b)^{-1}$ as $a \to 0$. The first two dots are at $a = 0.01$ and $a = 0.1$.

The phenomenon of a finite front speed in the limit of an infinitesimal exchange rate has been reported in other models of invasion dynamics. Lewis and Schmitz [21], for instance, considered a model of a population of individuals with two states—a diffusive state without reproduction, and an immobile state during which organisms reproduce. They also found that the invasion front speed approaches a finite value as the switching rate between the two states goes to zero. Another model was considered by Cook (see description in Ref. [2], Ch. 13) describing individuals who are always either stationary or diffusing, with each subpopulation reproducing according to a rate that depends on the total population. This model also exhibits a similar effect.

Before moving on to the model with diffusion, we briefly consider another limit. When $a = b \equiv g \to \infty$, the time spent by a typical particle on the GL is much smaller than the growth time, so the speed is determined by the fraction of time spent in the AL. Thus, $s^* \to 1/2$ as $g \to \infty$. When $a \neq b$, $s_\pm^* \to (1 + b/a)^{-1}$ as $a \to \infty$ (see also the discussion of the zero growth case in Appendix B 2).

In deriving results in Eqs. (4) and (5), no time-invariance of a front shape had to be assumed, only that it is "pulled." We see, however, that the decay rate in Eq. (5) is indeed a constant. If one seeks a uniformly translating front (UTF) solution for ρ and σ that depends on $x - st$, there is a continuous family of solutions, each characterized by a decay rate λ for a given s (details in Appendix A). The solution $(\lambda_\pm^*, s_\pm^*)$ obtained above is one point in this family. This suggests that the front evolves to a UTF form. The resulting UTF shapes match numerically obtained profile shapes.

IV. DIFFUSION—A COMPETING TRANSPORT MECHANISM

Although we could not solve the linearized equations when $\mathcal{D} \neq 0$, progress can be made with a UTF ansatz, which is justified numerically in Appendix A 4. Letting $\sigma(x,t) = \tilde{\sigma}(x - st)$ and $\rho(x,t) = \frac{a}{b}\tilde{\rho}(x - st)$—assumed to be valid in the vicinity of the front, linearizing the resulting equation around $(\tilde{\rho} = 0, \tilde{\sigma} = 0)$, and substituting an eigen-solution $\tilde{\rho} = Ae^{-\lambda z}$, $\tilde{\sigma} = Be^{-\lambda z}$ ($\lambda > 0$ describes the downwind front, and $\lambda < 0$, describes the upwind front), we obtain the following equation that relates the decay rate of the leading edge with speed s:

$$s\lambda = (1 - a) + \frac{ab}{b + (s - 1)\lambda} + \mathcal{D}\lambda^2. \tag{6}$$

The front "vicinity" can be defined by $|x - x_{\text{front}}| \lesssim 1/\lambda$, and x_{front} is a characteristic point on the front, such as the inflection point.

The resulting $s(\lambda)$ has multiple branches. The theory of pulled fronts [19] predicts that for ICs that decay faster than $e^{-\lambda_+^* x}$, with $\lambda_+^* > 0$ the minimum point of largest branch of $s(\lambda)$ ("steeply decaying" ICs), the selected decay rate of the downwind front will evolve to be λ_+^*, and its speed will be $s_+^* = s(\lambda_+^*)$ [22] (this was indeed so in the $\mathcal{D} = 0$ case). The resulting $s_+^*(a,b,\mathcal{D})$ is displayed in Fig. 4(a). Equivalently, the maximum of the lowest branch for $\lambda < 0$ describes the selected state (λ_-^*, s_-^*) of the upwind front resulting from steeply growing ICs, Fig. 4(b). We now study the properties of each front resulting from steep ICs, including a δ-function IC. We maintain $a,b \neq 0$, unless otherwise stated. The details of the calculations for the following discussion can be found in Appendix A. We first discuss the downwind front.

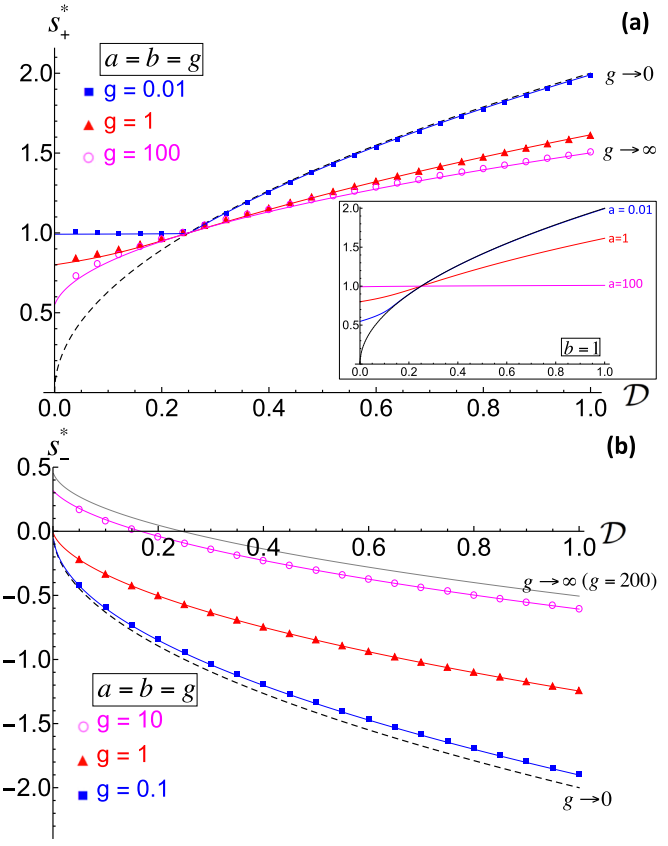

FIG. 4. The dimensionless speed of the downwind (a) and upwind (b) fronts vs. $\mathcal{D}$ for several coupling values. The symbols were obtained by numerical solutions of Eqs. (1) and (2), while continuous curves are theory—see main text. Dashed curves are $\pm 2\sqrt{\mathcal{D}}$—FKPP speed in units of v_0. We demonstrate in Appendix A 2 e that for $a/b = \text{const}$, $s_\pm^* \to \frac{a/b \pm 2\sqrt{\mathcal{D}}}{1 + a/b}$ for any $\mathcal{D}$ as $b \to \infty$.

A. Downwind front

1. *Fragility of the FKPP model*

The first key finding is the fragility of the FKPP model with respect to the perturbation by an independent advective mechanism. It turns out that as both a and $b \to 0$, $s_+^* \to 1$ for $0 \leqslant \mathcal{D} \leqslant 1/4$; see Appendix A 2 e. On the other hand, the front speed on the GL decoupled from the AL, i.e., the front speed in the FKPP model, is the well-known Fisher speed [3], given in the physical units by $s_F = 2\sqrt{D\delta} = 2v_0\sqrt{\mathcal{D}}$, or $2\sqrt{\mathcal{D}}$ in dimensionless units. This speed goes to zero as $\mathcal{D} \to 0$. Thus, an infinitesimal coupling of the FKPP model to an advective layer yields a finite change in the front speed. This effect takes place for $0 \leqslant \mathcal{D} < 1/4$, see Fig. 4(a), although the magnitude of the finite change due to an infinitesimal coupling decreases to zero as $\mathcal{D}$ approaches $1/4$. We will come back to the discussion of the range of $\mathcal{D}$ over which there is fragility, after discussing the crossover phenomenon. Note that $\mathcal{D} = 1/4$ is such $\mathcal{D}$ at which the Fisher speed equals the advective speed.

Similarly, the decay rate of the front also undergoes a finite change under an infinitesimal coupling from the FKPP decay rate $1/\sqrt{\mathcal{D}}$ to $(1 - \sqrt{1 - 4\mathcal{D}})/(2\mathcal{D})$ for $0 \leqslant \mathcal{D} \leqslant 1/4$; see Appendix A 2 e.

Thus, we find that the FKPP model is fragile with respect to the coupling to the AL, i.e., such perturbation is singular [23].

Whereas the FKPP model is fragile with respect to the coupling to the AL, the $\mathcal{D} = 0$ model is not fragile with respect to the addition of the diffusion term on the GL. Adding diffusion in the GL does not change s_+^* discontinuously for any combination of coupling values, and s_+^* remains finite as $\mathcal{D}$ becomes non-zero—see Fig. 4(a). We show directly with perturbation theory in Appendix A 2 b, that when the Fisher speed of the GL is much less than the advective speed (i.e., when $\mathcal{D} \ll 1/4$),

$$s_+^* \approx s_+^*(\mathcal{D} = 0) + \frac{b}{1 + \sqrt{a}}\mathcal{D}. \tag{7}$$

The same can be said about the decay rate, which is given by

$$\lambda_+^* \approx \lambda_+^*(\mathcal{D} = 0) + c\mathcal{D}, \tag{8}$$

where c is given in Appendix A 2 b. Thus, at small diffusion, the front speed and shape are given approximately by the speed and shape if only the advective mechanism was operating; the advective mechanism dominates at small $\mathcal{D}$ and finite a and b. Moreover, we just saw that this speed does not go to zero as either a or $b \to 0$, which again leads to the idea of fragility with respect to the coupling.

The reason why s_+^* is continuous with an infinitesimal perturbation by $\mathcal{D}$ may be viewed as a consequence of the finite speed in the diffusion-free model (for any $a,b \neq 0$). As $\mathcal{D} \to 0$, the diffusive-only transport mechanism (zero coupling) is infinitely slower than the advective-only mechanism (zero $\mathcal{D}$) [24]. When both are present, the advection dominates.

At this stage we would like to draw the reader's attention to an important point. Note that if an advective term $-v_1 \frac{\partial \sigma}{\partial x}$ with constant v_1 were present in Eq. (2), it can be removed by changing the reference frame, while modifying v_0 in Eq. (1) (we have focused on $\mathbf{v} = v_0 = const$ in this paper). In other words, it is not possible to remove an advective term from the model entirely—only to move it from one layer to another. In contrast, if the same constant velocity advective term was present in the FKPP model, the same transformation would remove this term. Thus, whereas the effect of an advective term with a constant velocity on the front speed is purely additive in the basic FKPP model, this is not the case in our model, since an advective term cannot be removed by a simple Gallilean transformation. Therefore, there is a genuine competition between the two transport mechanisms. Coupling opens up an alternative "transport channel."

The fragility effect is an example of the consequence of this competition. For $\mathcal{D} < 1/4$, the Fisher speed is lower than the advective speed, and for $\mathcal{D} > 1/4$, it is greater. So, it appears that in the limit of both a and b being infinitesimal, the downwind front speed is given by the greater of the speeds due to either of the two mechanisms considered separately; see Fig. 4(a). But this will not always be the case, as we will see when examining another route to fragility below.

2. *Effective FKPP description at large $\mathcal{D}$*

The linear dependence of s_+^* on $\mathcal{D}$ at small $\mathcal{D}$, demonstrated in Eq. (7), indicates that our model cannot be mapped to an FKPP model—which exhibits the $\sim\sqrt{\mathcal{D}}$ scaling. On the other hand, at large $\mathcal{D}$ it is possible to map our model to an FKPP model, and there exists an asymptotic behavior,

$$s_+^* \sim v_{\text{eff}} + 2\sqrt{\mathcal{D}_{\text{eff}}}, \tag{9}$$

where $\mathcal{D}_{\text{eff}} \propto \mathcal{D}$. We recognize this to be s_+^* of the model $\dot{\sigma} = -v_{\text{eff}}\sigma' + \mathcal{D}_{\text{eff}}\sigma'' + f(\sigma)$, which is just an FKPP model with advection.

To discover this asymptotic behavior of s_+^*, and to obtain the dependence of v_{eff} and $\mathcal{D}_{\text{eff}}$ on parameters, we noticed that the relevant branch of $s(\lambda)$ approaches $s(\lambda)$ of the basic FKPP model as $\lambda \to \infty$ and that both solutions also behave as λ^{-1} at small λ. Now, FKPP $\lambda_\pm^* = \pm\frac{1}{\sqrt{\mathcal{D}}}$, so we considered an ansatz:

$$\lambda_\pm^* = \pm\frac{c_1(a,b)}{\sqrt{\mathcal{D}}} + \frac{c_2(a,b)}{\mathcal{D}} + \cdots, \tag{10}$$

which allows us to solve for the coefficients c_i order-by-order that makes such $\lambda_\pm^*$ an extremum of the relevant branch of $s(\lambda)$. It is important to stress that this is an asymptotic ansatz for a large-$\mathcal{D}$ regime. When we stop at the leading term, and substitute this into the appropriate branch of $s(\lambda)$, we get the result in Eq. (9). Including the next term in Eq. (10) would introduce a $O(1/\sqrt{\mathcal{D}})$-correction to Eq. (9). The details can be found in Appendix A 2 a.

The resulting $\mathcal{D}_{\text{eff}} \to \mathcal{D}$ and $v_{\text{eff}} \to 0$ when $a \to 0$ at $b =$ const or $b \to \infty$ at $a =$ const, i.e., particles are forced to stay on the GL and the predictions match those of the FKPP model without advection. On the other hand, $\mathcal{D}_{\text{eff}} \to 0$ and $v_{\text{eff}} \to 1$ as $a \to \infty$ at $b =$ const or $b \to 0$ at $a =$ const > 1, i.e., particles are forced to stay on the AL.

Generally, the functions $\mathcal{D}_{\text{eff}}$ and v_{eff} have a complicated dependence on parameters a and b. However, sufficiently far from $(a = 1, b = 0)$, $c_1 \approx 1$, which gives

$$\mathcal{D}_{\text{eff}} \approx \frac{[2 - a - b + \sqrt{(a+b)^2 + 4(1+b-a)}]^2}{16}\mathcal{D}, \tag{11}$$

$$v_{\text{eff}} \approx \frac{1}{2} + \frac{a - b - 2}{2\sqrt{(a+b)^2 + 4(1+b-a)}}. \tag{12}$$

A more accurate approximation can be found in Appendix A 2 a. The role of the special point $(a = 1, b = 0)$ will become clear as we discuss the crossover phenomenon.

3. *Crossovers and anomalous front width*

Thus far, we have found that at small $\mathcal{D}$ the downwind front properties are dominated by the AL, while at a large $\mathcal{D}$, this front behaves as in the FKPP model with advection, with an effective v_{eff} and $\mathcal{D}_{\text{eff}}$. There is a crossover between these two asymptotic regimes at some intermediate $\mathcal{D}$. At a and $b \ll 1$, this crossover is sharp and takes place at $\mathcal{D} = 1/4$ (sharp means the width of the crossover region is very small, i.e., the asymptotics on both sides remain valid right up to the crossover point; it does not refer to the discontinuity of derivatives). In order for the crossover to penetrate to a given value of $\mathcal{D}$ when $\mathcal{D} \ll 1/4$, the parameter b has to scale as $\mathcal{D}^{-1/2}$; this also applies to the upwind front. In other words, at a fixed $\mathcal{D}$, the FKPP-like regime can be reached by increasing b. Details on the crossover can be found in Appendix A 2 e.

For a generic set of a and b, the characteristic crossover point takes place at some finite $\mathcal{D}$. However, there exists one special parameter combination when this crossover point diverges, and thus, there is no mapping to the FKPP-like behavior at any finite $\mathcal{D}$. It turns out that when $a = 1$, $c_1 \sim b^{1/4}$ for small b, so $c_1 \to 0$ as $b \to 0$. The leading order behavior of λ_+^* becomes $\sim 1/\mathcal{D}$. Whenever λ_+^* does not scale like $\sim 1/\sqrt{\mathcal{D}}$, s_+^* will not scale like $\sim\sqrt{\mathcal{D}}$. At any fixed nonzero a and b, increasing $\mathcal{D}$ eventually causes the first term in Eq. (10) to be the leading term, and Eq. (9) becomes valid. At $a = 1$, the closer b is to zero, the larger this crossover $\mathcal{D}$ is, and it diverges as $b^{-1/2}$ at $a = 1$.

The results outlined in the last paragraph arise from the following analysis. As b is decreased at $a = 1$, λ_+^* crosses over from scaling like $\sim b^{1/4}\mathcal{D}^{-1/2}$ to saturating at $\sim\mathcal{D}^{-1}$ (we can talk about a crossover $\mathcal{D}$ at fixed b or a crossover b at fixed $\mathcal{D}$—it refers to the crossover between the same pair of regimes). Thus, there is an anomalous growth—but not divergence—of the front width ($\propto 1/\lambda_+^*$) as b is decreased below this crossover. Equating the above two scaling regimes, we see that the crossover b decreases as $\sim\mathcal{D}^{-2}$ when $\mathcal{D}$ is increased, and thus the crossover $\mathcal{D}$ grows as $b^{-1/2}$ at small b. We remind the reader that this concerns the asymptotic theory

for large $\mathcal{D}$. More details and numerical verification of these ideas can be found in Appendices A 2 a and A 2 e.

In summary of the crossover phenomenon, the space of parameters $\mathcal{D}$, a, b can be subdivided into a region where the front behaves in the FKPP-like manner—for example, $s_+^* \sim \sqrt{\mathcal{D}}$, and a region where it does not. The surface of the crossover $\mathcal{D}$ versus a, and b can be complicated. At $a = 1$ and small b, the slice of this crossover surface is given by $\mathcal{D}_{\text{crossover}} \propto b^{-1/2}$ (or equivalently, $b_{\text{crossover}} \propto \mathcal{D}^{-2}$). The exact pre-factor is somewhat ambiguous and depends on a definition of a crossover point. The FKPP-like behavior can be found above this "crossover curve"—at large $\mathcal{D}$ and b—where $\lambda_+^* \sim b^{1/4}\mathcal{D}^{-1/2}$, and the non-FKPP behavior can be found below this curve, where $\lambda_+^* = \mathcal{D}^{-1}$. The characteristic front width is $1/\lambda_+^*$. Thus, by decreasing b at fixed $\mathcal{D}$, the front width grows until reaching some constant value as we go past this crossover boundary. In the original variables, this trajectory in the $\mathcal{D}$-b space is followed if b is lowered by decreasing β at fixed δ, D and v_0. If this boundary is crossed along some other curve in the $\mathcal{D}$-b space (at $a = 1$), the front width may instead decrease. For example, if b is lowered by increasing δ, while holding D, v_0, and β fixed, then $\mathcal{D}$ will not be constant, and we follow along the curve $\mathcal{D}(b) = \frac{D\beta}{v_0^2 b}$. As we cross the crossover boundary to enter the FKPP regime $\lambda_+^* \sim b^{1/4}\mathcal{D}^{-1/2}$, we see that $\mathcal{D}$ increases in such a way that the front width actually decreases as $\sim\delta^{-1/4}$ in the physical length units (such as meters). Similar thinking can be applied to the upwind front discussion in Sec. IV B.

4. *Fragility revisited*

Before moving on to discuss the phenomenology for the upwind front, we briefly return to the subject of fragility. We saw above that when both a and b are changed from zero (i.e., it is a perturbation from the FKPP model) to an infinitesimal value, the downwind front speed and decay rate change by a finite amount, as long as $\mathcal{D} < 1/4$, which is just the crossover point when both $a \ll 1$ and $b \ll 1$. There exists another route for breaking predictions of the FKPP model by an infinitesimal perturbation. Consider a finite value of b, but $a = 0$. If the IC is nonzero only on the GL, ρ will be zero, so this is also equivalent to the FKPP model. If we now let a be infinitesimal, s_+^* has a finite difference from $2\sqrt{\mathcal{D}}$ for $\mathcal{D} < \frac{1}{4(1+b)}$, which is the new crossover point. This is discussed in Appendix A 2 e. Thus again, the FKPP model is fragile with respect to this type of coupling to the independent advective process as long as $\mathcal{D}$ is below the crossover. This crossover is also sharp, in the sense stated above. It is important to point out that for $\mathcal{D}$ below this value, the speed of the front is a function of $\mathcal{D}$—see Appendix A 2 e, and also the small-a curve in the inset of Fig. 4(a), where it is clear that s_+^* is a function of $\mathcal{D}$ before it merges unto $2\sqrt{\mathcal{D}}$. Thus, it is no longer the case that the speed is simply the greater of the speeds due to either of the two mechanisms considered separately—diffusion only (FKPP), or advection only ($\mathcal{D} = 0$ model). On the other hand, $s_+^*(\mathcal{D})$ is a continuous function that starts at $(1 + b)^{-1}$ at $\mathcal{D} = 0$ (when $a \to 0$) and goes to $2\sqrt{\mathcal{D}}$ at the crossover point, after which it is given by $2\sqrt{\mathcal{D}}$. So, the larger is the value of $\mathcal{D}$, the more we depart from the $\mathcal{D} = 0$ result, while the magnitude of the finite change due to the infinitesimal coupling becomes smaller, and vanishes at the crossover point. Hence, there is a tradeoff between the magnitude of the finite change in the speed due to an infinitesimal coupling (fragility) and the importance of the cooperation between the two transport mechanisms.

B. Upwind front and divergent front width

Similar phenomena happen for the upwind front—where the two transport mechanisms are opposing, but there are some notable differences. Figure 4(b) can serve as a reference for this discussion. Following the similar procedure as described above, we find that there is a large $\mathcal{D}$ asymptotic form,

$$s_-^* \sim v_{\text{eff}} - 2\sqrt{\mathcal{D}_{\text{eff}}}, \tag{13}$$

except at $(a = 1, b \to 0)$, with identical $c_1(a,b)$, $\mathcal{D}_{\text{eff}}(a,b)$, and $v_{\text{eff}}(a,b)$ as for the downwind front. This is s_-^* of the model $\dot{\sigma} = -v_{\text{eff}}\sigma' + \mathcal{D}_{\text{eff}}\sigma'' + f(\sigma)$. At $a = 1$, $s_-^* \approx -\frac{3b^{1/3}\mathcal{D}^{2/3}}{2^{2/3}}$ at small $\mathcal{D}$ before crossing over into $\sim -\sqrt{\mathcal{D}}$ behavior. As was the case with the downwind front, this crossover $\mathcal{D}$ again diverges as $b^{-1/2}$ when $b \to 0$. Equivalently, the crossover b decreases as $\mathcal{D}^{-2}$ in the asymptotically large $\mathcal{D}$ limit. However, now the second term in the series in Eq. (10) does not protect λ_-^* from remaining finite. Using a different method for finding λ_-^*, we learned that λ_-^* crosses over from the $\sim b^{1/4}\mathcal{D}^{-1/2}$ to $\sim(b/\mathcal{D})^{1/3}$ scaling as b decreases. Thus, the upwind front width diverges at $a = 1$ as $\sim b^{-1/3}$ when $b \to 0$ at a fixed $\mathcal{D}$, and $(a = 1, b = 0)$ is a critical point.

As with the downwind front, adding diffusion to the GL also does not change s_-^* discontinuously—see Fig. 4(b). Advection alone cannot propagate the upwind front for $a < 1$, so diffusion is essential for front movement. For a slightly below 1 and $\mathcal{D} \ll \frac{(1-a)^3}{27b^2}$, $s_-^* \sim -2\sqrt{1-a}\sqrt{\mathcal{D}}$. For $a > 1$ and in the absence of diffusion, the front propagates in the direction of the wind, so s_-^* is positive. For small $\mathcal{D}$, it is given by

$$s_-^* \approx s_-^*(\mathcal{D} = 0) - \frac{b}{\sqrt{a} - 1}\mathcal{D}. \tag{14}$$

Details concerning the small-$\mathcal{D}$ regime can be found in Appendix A 2 b. As $\mathcal{D}$ is increased further, the direction of the propagation reverses for $\mathcal{D} > \mathcal{D}_{\text{stall}}$—see Appendix A 2 c. Exactly at $\mathcal{D}_{\text{stall}}$ this front does not move. $\mathcal{D}_{\text{stall}}$ increases with a and decreases with b. For small $a - 1 > 0$, $\mathcal{D}_{\text{stall}} = (a-1)^3/(8b^2)$. Using Eqs. (11)–(13), we see that at large a and b, $\mathcal{D}_{\text{stall}} \sim (\frac{a}{2b})^2$, so when $a/b = \text{const}$, $\mathcal{D}_{\text{stall}}$ has a limiting value.

A prominent feature of Fig. 4(a) is the intersection at $\mathcal{D} = 1/4$, where s_+^* is coupling-independent. This can happen if $a\rho = b\sigma$ for all x [see Eqs. (1) and (2)], which is only possible at $\mathcal{D} = 1/4$, when Fisher speed = advective speed. To see that $a\rho$ does equal to $b\sigma$ at $\mathcal{D} = 1/4$, we can show that for ICs that evolve to a UTF, $s_+^* = 1$ for any a or b only when $\mathcal{D} = 1/4$. Then it follows from one of the equations for the UTF profile that $a\rho = b\sigma$ [see Eq. (A1)] [25]. The point $\mathcal{D} = 1/4$ can be thought of as a robust operating condition of the catalyst.

V. DISCUSSION

We have considered in this paper a model in which a reaction-diffusion process is coupled to an independent advective process. In contrast to a reaction-diffusion model with a constant-velocity advective term—where the role of advection on the speed of the reaction front is purely additive—here diffusion and advection by a constant velocity do not take place simultaneously. This leads to a competition between the two transport mechanisms.

We found that the mapping to an effective FKPP model with advection is generally possible only at large desorption rates or at fast diffusion. We also saw that there is a complicated crossover phenomenology from the FKPP-like regime to a non-FKPP-like regime. Most importantly, we found that the FKPP model can be fragile with respect to the coupling to an independent advective process—giving a finite change in front properties from an infinitesimal coupling. This happens as long as $\mathcal{D}$ is between zero and a certain value, which depends on the way in which this coupling was realized. Moreover, we found a critical point, approaching which causes divergence of the upwind front width, and an anomalous growth of the downwind front width. It also deserves to note that coupling of the FKPP to the AL renormalizes even a very large $\mathcal{D}$, so the AL can never be ignored!

Fragility was uncovered in this work through the discussion of a finite change due to an infinitesimal perturbation as a certain parameter is increased from below. However, there is an alternative view of fragility that does not require infinitesimal perturbations, and may instead be viewed as the limiting behavior as this parameter is increased from above. Consider, for instance, the case of $a = b = g$. For $g = 0.1$ there exists some function $s_+^*(\mathcal{D})$. Lowering g to 0.01 will cause some change in $s_+^*(\mathcal{D})$. Lowering g to 0.001 will cause a smaller change in $s_+^*(\mathcal{D})$, and so on, until there is some limiting function that is different from the case of $g = 0$.

The coupling to the AL introduces two effects. First, it takes particles out of the reactive substrate for some characteristic time. Second, it advects them, and causes the competition between the two transport mechanisms. To understand the relative role of these two effects in causing the rich phenomenology, we considered a model with the advection removed from the AL. Thus, in this alternative model, particles are either participating in the reaction-diffusion process, or they do nothing over some characteristic time—the AL now acts like an immobile storage space. This is described in Appendix A 3. We found that in this model, both the upwind and the downwind front widths diverge as $\sim b^{-1/4}$ at small b when $a = 1$ and $\mathcal{D}$ is arbitrary. There is no symmetry breaking by advection, so both fronts are mirror images of each other. However, front speeds behave as $s_\pm^* \propto \sqrt{\mathcal{D}}$ for any $\mathcal{D}$, so there is no fragility, and no crossover between the FKPP-like and the non-FKPP-like regime. These findings are understandable—with zero coupling, the model is FKPP, and with an infinitesimal coupling, the front speed is still limited by diffusion—as $\mathcal{D}$ goes to zero, so must the front speed. Infinitesimal coupling cannot lead to a finite speed change because there is no other mechanism to overtake the transport, i.e., there is no opening of an alternative transport channel.

These findings force us to conclude that the fragility and complex crossover phenomenology found here are results of the competition between two transport mechanisms. On the other hand, the diverging front width at $(a = 1, b \to 0)$ is a result of particles temporarily leaving the reactive substrate. We thus speculate that this is a less generic effect, and may not survive if reactions are introduced into the AL. However, the first two findings—especially the fragility of reaction-diffusion predictions—are a generic consequence of competing transport mechanisms, and similar effects may take place when a reaction-diffusion process is expanded in a way that involves a competing advective transport channel ([2,10–18,26]).

ACKNOWLEDGMENTS

We thank David Schneider, whose insights and feedback has greatly influenced and improved this work; M. C. Cross for valuable comments; S. H. Strogatz, David R. Nelson, Thiparat Chotibut, N. Mahowald, W. van Saarloos, Stephen Ellner, and Alan Hastings for useful discussions. We also thank Saad E. Hebboul, whose editorial comments have lead to a significant expansion of the scope of this paper. This work was supported in part by a grant from the Science & Technology Directorate, Department of Homeland Security, which was administered via an Interagency Agreement with our collaborators in the USDA (Interagency Agreement No. HSHQDC-10-X-00138), and a seed grant from the Atkinson Center for a Sustainable Future at Cornell University.

APPENDIX A: UNIFORMLY TRANSLATING FRONTS (UTF)

Substituting the UTF ansatz $\sigma(x,t) = \tilde{\sigma}(x - st)$ and $\rho(x,t) = \frac{a}{b}\tilde{\rho}(x - st)$ into Eqs. (1) and (2) of the main text yields

$$(1 - s)\frac{d\tilde{\rho}}{dz} = -b\tilde{\rho} + b\tilde{\sigma}, \tag{A1}$$

$$-s\frac{d\tilde{\sigma}}{dz} = f(\tilde{\sigma}) - a\tilde{\sigma} + a\tilde{\rho} + \mathcal{D}\frac{d^2\tilde{\sigma}}{dz^2}, \tag{A2}$$

where $z = x - st$. This is a three-dimensional dynamical system in coordinates $\tilde{\sigma}$, $\tilde{\rho}$, and $\tilde{u} = \frac{d\tilde{\sigma}}{dz}$, and has fixed points at $(\tilde{\sigma} = 0, \tilde{\rho} = 0, \tilde{u} = 0)$ and $(\tilde{\sigma} = 1, \tilde{\rho} = 1, \tilde{u} = 0)$, which are, respectively, stable and unstable (note: t decreases with increasing z). Only the heteroclinic solution connecting the two goes from $z = -\infty$ to $z = +\infty$, so $\rho(x)$ or $\sigma(x)$ will have a sigmoidal shape. Thus, if an IC evolves to a UTF, it will be a front-like solution. The existence of stationary solutions, such as section I in Fig. 2(a) of the main text, implies that a UTF cannot exist for all x and t, so a UTF describes the vicinity of a moving front, defined more precisely below.

Solutions of nonlinear Eqs. (A1) and (A2) are parametrized by s, which determines the phase portrait in the $(\tilde{\rho}, \tilde{\sigma})$ space. It is customary to characterize solutions by the eigenvalues around the state (0,0), which describes the tail of a UTF. Instead of expressing the eigenvalues as functions of s, we follow the standard convention [19] and express s as a function of eigenvalue $\equiv \lambda$. It is easiest to do this by linearizing Eqs. (A1) and (A2) around $(\tilde{\sigma} = 0, \tilde{\rho} = 0)$, and substituting

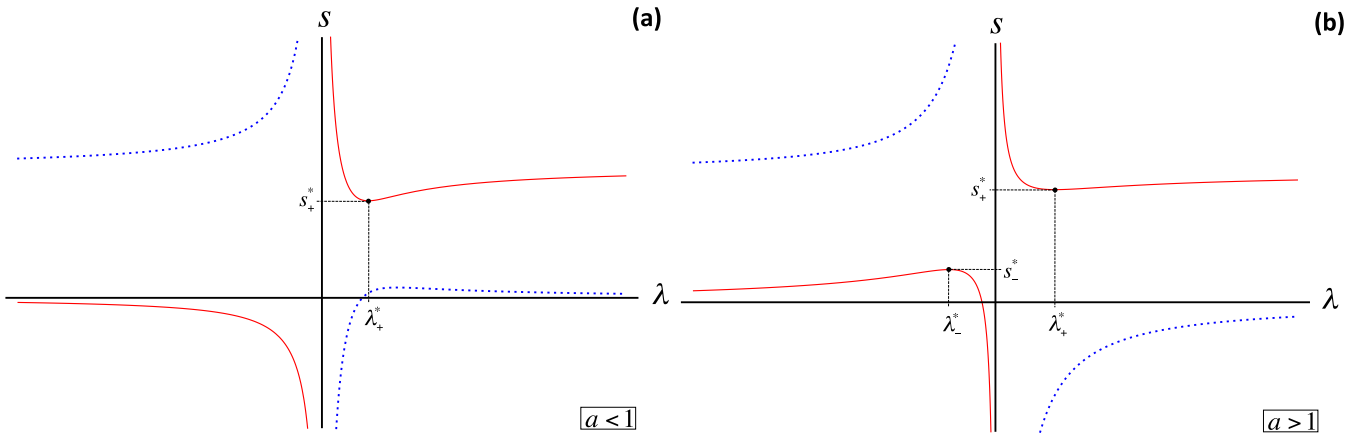

FIG. 5. Typical structure of the branches $s_1(\lambda)$—red solid curve, and $s_2(\lambda)$—blue dotted curve. Here $a < 1$ in panel (a) and $a > 1$ in panel (b). The points (λ^*_+,s^*_+) and (λ^*_-,s^*_-) are also noted. The qualitative picture remains for any $b > 0$. The value of λ^*_- goes to $-\infty$ as $a \to 1$ from above, and stays at $-\infty$ for $a < 1$, corresponding to a lack of propagation of the upwind front for $a < 1$. There is a horizontal asymptote always taking place at $s = 1$.

an eigen solution $\tilde{\rho} = Ae^{-\lambda z}$, $\tilde{\sigma} = Be^{-\lambda z}$. The result is

$$s\lambda = (1-a) + \frac{ab}{b+(s-1)\lambda} + \mathcal{D}\lambda^2. \tag{A3}$$

There are two solutions, which we label $s_1(\lambda)$ and $s_2(\lambda)$. We devote the rest of this section to the study of Eq. (A3).

1. Zero diffusion

When $\mathcal{D} = 0$, $s_1(\lambda)$ and $s_2(\lambda)$ are given explicitly by

$$s_{1,2}(\lambda) = \frac{1-a-b+\lambda \pm \sqrt{(\lambda-1+a-b)^2+4ab}}{2\lambda}, \tag{A4}$$

with s_1 is the $+$ solution and s_2 is the $-$ solution. These relations give the speed as a function of the decay rate of the solution. This is plotted in Fig. 5. Note that positive λ describe a downwind front—it decays with increasing x, while the negative λ describe the upwind front, which grows with increasing x.

Profile shapes computed as heteroclinic trajectories of the system in Eqs. (A1) and (A2) are displayed in Fig. 18 (Appendix E 3) for two sets of parameters.

The question of the selected (λ,s) from a given IC is a problem in front selection. In this work, we focused on ICs with a finite support, including a δ-function. The extremal points of $s(\lambda)$ take place precisely at the locations predicted by Eqs. (4) and (5) in the main text, $(\lambda^*_\pm,s^*_\pm)$, derived in Appendix B without requiring a UTF assumption; that prediction remains true for any IC with a finite support (see Appendix C below). The reason that the extrema of $s(\lambda)$ are located at these $(\lambda^*_\pm,s^*_\pm)$ is not coincidental, but is consistent with the general theory of fronts [19] in the long-time asymptotic regime.

The review on front propagation [19] states that sufficiently steep ICs will select the leading front (i.e., decaying with increasing x) with a characteristic decay rate being the $\lambda > 0$ at which the minimum point of the top-most branch of $s(\lambda)$ occurs, and the speed is given by s at that λ. The exception—corresponding to "pushed" fronts—occurs when there exists a nonlinear solution that at low density matches exactly the eigen-solution with the nonminimum eigenvalue, but this is a rather special case.

The discussion in Ref. [19] was based on the leading front (i.e., decaying with increasing x). However, the trailing front propagating with a certain speed s becomes a leading front propagating with the speed $-s$, i.e., $\lambda \to -\lambda$ and $s \to -s$, upon the spatial mirror-reflection. Therefore, steep ICs will select the trailing front with a characteristic growth rate being the $\lambda < 0$ at which the maximum point of the bottom-most branch of $s(\lambda)$ occurs. As already mentioned, our study of the upwind front for $\mathcal{D} = 0$ confirmed this. For $\mathcal{D} \neq 0$, this has also been verified against numerical simulations of the model and supported by saddle-point calculations in Appendix C.

The notation (s^*,λ^*) will now be used in two ways—denoting the position of the extrema of $s(\lambda)$, as well the properties of the selected state.

Having defined the characteristic width of the front by the eigenvalues λ, we can say what the "vicinity" of the front is: it is a region of $|x - x_{\text{front}}| \lesssim 1/|\lambda|$, where x_{front} can be defined, for example, as the inflection point of $\rho(x,t)$ or $\sigma(x,t)$, although the precise definition is unimportant.

We can also heuristically argue that a front converges to a UTF. The speed and decay rate of the leading edge of a solution to Eqs. (1) and (2) of the main text, is selected by the IC. However, if the initial evolution leads to a UTF, the front width of the full, nonlinear profile can be estimated from the eigenvalue $\lambda(s)$ of solutions to Eqs. (A1) and (A2) around the attractor at (0,0). Although these are obtained from the linearization of Eqs. (A1) and (A2), they are properties of the solutions of the full, nonlinear profile. On the other hand, we have obtained the speeds $s^*_\pm$ and the widths $\lambda^*_\pm$ [Eqs. (4) and (5) of the main text] for a specific IC without assuming a UTF. As already mentioned, these $(\lambda^*_\pm,s^*_\pm,)$ lie on the $\lambda(s)$ curve produced by the UTF assumption. Although not a rigorous proof, it is an argument for the solution to approach a UTF.

2. Nonzero diffusion

Below we plot $s(\lambda)$ curves when $\mathcal{D} \neq 0$; Fig. 6 is for $a < 1$ and Fig. 7 is for $a > 1$. These figures do not all have the same

scale—they are meant to demonstrate qualitative changes in the structure of $s(\lambda)$ as parameters a and $\mathcal{D}$ vary (the parameter b was set to 1 in these figures). These plots are meant to demonstrate the evolution of the branches of $s(\lambda)$ from the $\mathcal{D}=0$ case, seen in Fig. 5. The black dashed curve represents $\mathcal{D}\lambda+\lambda^{-1}=s_{\rm FK}(\lambda)$ of the single-variable FKPP model $\dot{\phi}=f(\phi)+\mathcal{D}\frac{d^2\phi}{dx^2}$. The selected downwind speed that appears in Fig. 4(a) of the main text is taken from the minimum of the top solid (red) curve for $\lambda>0$, whereas the selected upwind speed that appears in Fig. 4(b) of the main text is taken form the maximum of the bottom solid (also red) curve for $\lambda<0$.

We next study the extrema of $s_1(\lambda)$ analytically in the regime of large and small $\mathcal{D}$. We will continue to use the extremal points of $s(\lambda)$ to predict the selected states $(\lambda^*_\pm, s^*_\pm)$ from a compact IC. When $\mathcal{D}\neq 0$, $s_1(\lambda)$ and $s_2(\lambda)$ are given explicitly by

$$s_{1,2}(\lambda)=(1-a-b+\lambda+\mathcal{D}\lambda^2\pm\sqrt{\psi})/(2\lambda), \quad \text{(A5)}$$

$$\text{where}\quad \psi=a^2+2a(b-\mathcal{D}\lambda^2+\lambda-1)+[1+b+\lambda(\mathcal{D}\lambda-1)]^2,$$

with s_1 is the $+$ solution and s_2 is the $-$ solution. The solution $s_1(\lambda)$ describes the aforementioned solid red branch in Figs. 6 and 7, i.e., is the largest solid branch for $\lambda>0$ and the lowest solid branch for $\lambda<0$. We are interested in the minimum of this branch for $\lambda>0$ and maximum for $\lambda<0$. We have

$$\frac{ds_1}{d\lambda}=\left\{\frac{\lambda(2\mathcal{D}\lambda-1)[-a+b+\lambda(\mathcal{D}\lambda-1)+1]}{\sqrt{\psi}}-\sqrt{\psi}+a+b+\mathcal{D}\lambda^2-1\right\}\Big/(2\lambda^2). \quad \text{(A6)}$$

Over the next several pages we discuss asymptotic scaling behaviors and their crossovers for $\lambda^*_\pm$ and $s^*_\pm$, separating the discussion into large-$\mathcal{D}$ and small-$\mathcal{D}$ regimes, as defined below.

a. Large $\mathcal{D}$

We would like to find λ^* that satisfy $\frac{ds_1}{d\lambda}=0$. For a purely FKPP model, the solutions are $\lambda^*_\pm=\pm\frac{1}{\sqrt{\mathcal{D}}}$. Note that $\lambda^{-1}+\mathcal{D}\lambda$ is the asymptote of the full solution in Eq. (A5) at large λ, and they both vary like $\sim\lambda^{-1}$ at small λ (and finite a,b), so the positions of the extrema of $\lambda^{-1}+\mathcal{D}\lambda$ should serve as a first guess for the positions of extrema in the full problem. In fact, we noticed numerically that the extrema in the full problem at large $\mathcal{D}$ usually do lie very close to the extrema of the FKPP

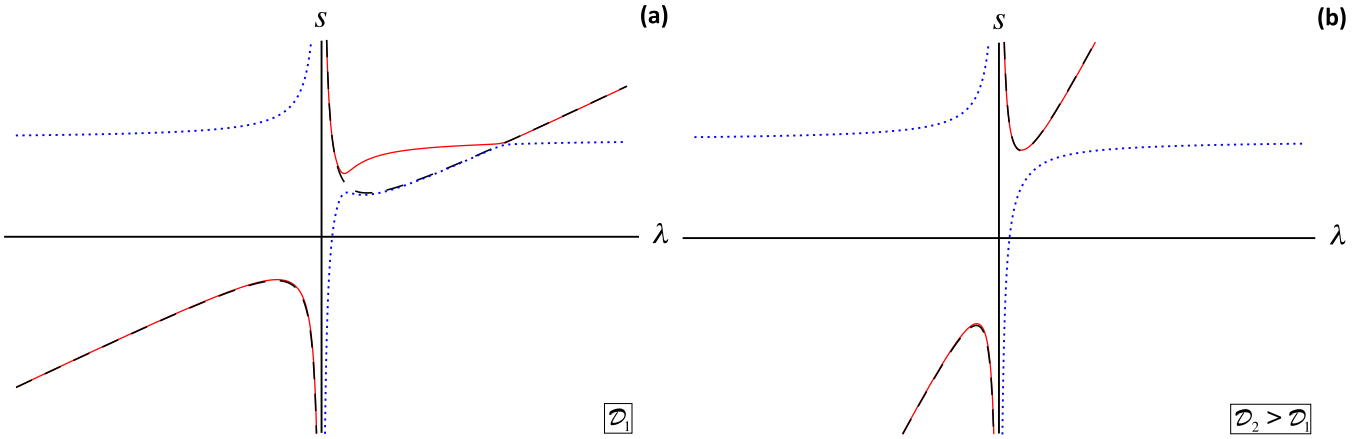

FIG. 6. Typical structure of the branches of $s(\lambda)$ when $a<1$ and $\mathcal{D}\neq 0$. Red solid curve is $s_1(\lambda)$, and blue dotted curve is $s_2(\lambda)$. The black dashed curve represents $\mathcal{D}\lambda+\lambda^{-1}$ from the FKPP model. In panel (b), $\mathcal{D}$ was chosen to be greater than in panel (a).

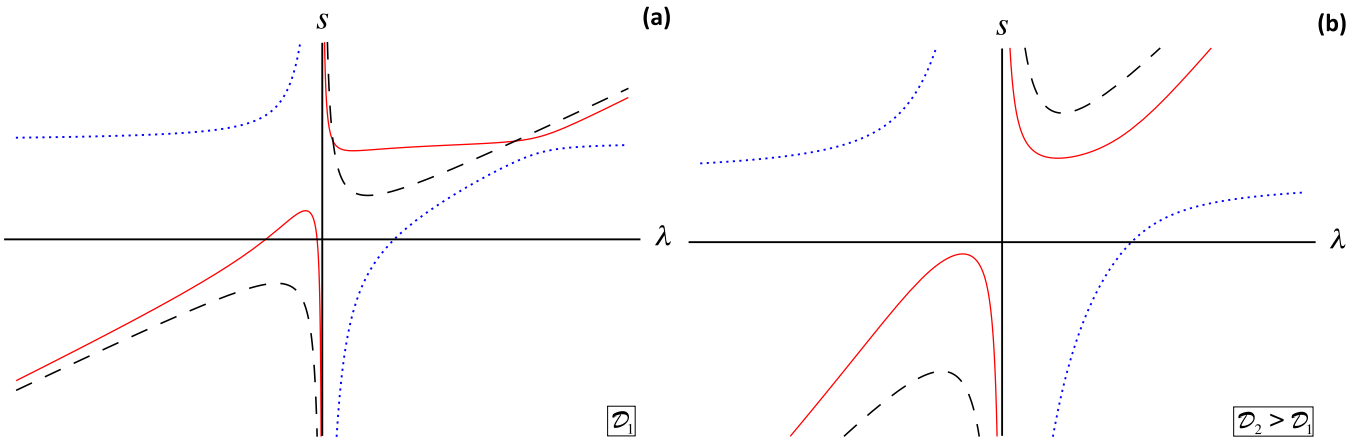

FIG. 7. Typical structure of the branches of $s(\lambda)$ when $a>1$ and $\mathcal{D}\neq 0$. Red solid curve is $s_1(\lambda)$, and blue dotted curve is $s_2(\lambda)$. The black dashed curve represents $\mathcal{D}\lambda+\lambda^{-1}$ from the FKPP model. In panel (b), $\mathcal{D}$ was chosen to be greater than in panel (a).

model. This suggests an ansatz

$$\lambda^*_\pm = \pm\frac{c_1}{\sqrt{\mathcal{D}}} + \frac{c_2}{\mathcal{D}} + \cdots \tag{A7}$$

The $\sim\mathcal{D}^{-1/2}$ leading behavior of both λ^*_+ and λ^*_- at large $\mathcal{D}$ has been verified from the numerically computed extrema of $s_1(\lambda)$ from Eq. (A5). The coefficients c_1, c_2, etc. can be found iteratively—first seek the coefficient of the first term, by substituting $\lambda^* = \pm\frac{c_1}{\sqrt{\mathcal{D}}}$ into Eq. (A6), expanding in $\frac{1}{\sqrt{\mathcal{D}}}$, and solving for c_1 that eliminates the $\mathcal{D}^0$ term in this expansion. By doing this, we find a c_1 that makes this ansatz asymptotically exact as $\mathcal{D}\to\infty$; i.e., it will give us a large-$\mathcal{D}$-approximation to λ^* for arbitrary a and b. We may then repeat this with the second term in Eq. (A7) included, and seek c_2 that eliminates the $\mathcal{D}^{-1/2}$ term—it will improve the asymptotic approximation to the true λ^*, make it more accurate down to smaller $\mathcal{D}$, and so on. This method will work as long as λ^* does not become infinite for any parameter values (and thus, none of the c_is become infinite for any parameter values), but we know this because as we just mentioned, $\mathcal{D}\lambda$ is the asymptote of the full solution in Eq. (A5) at large λ; i.e., there is a tail of $s_1(\lambda)$ that is independent of a and b.

When this procedure was implemented, the following solution for c_1 was found with the help of Mathematica,

$$c_1(a,b) = \sqrt{\frac{(2+a+b)^2 - (1+2a+2b)\chi^{1/3}(a,b) + \chi^{2/3}(a,b)}{3\chi^{1/3}(a,b)}}, \quad \text{where}$$

$$\chi(a,b) = a^3 + 3a^2(2+b) + (2+b)^3 + 3a(b-1)(b+5) - 27a + 6i\sqrt{3}\sqrt{a^4 + 3a^3(2+b) + a(2+b)^3 + 3a^2(b-1)(b+5)}. \tag{A8}$$

So at the lowest order in $\frac{1}{\sqrt{\mathcal{D}}}$, the coordinates of the two extrema, λ^*_+ and λ^*_-, remain symmetric about 0. In contrast, c_2 is identical for both fronts, so overall λ^*_+ and λ^*_- are slightly asymmetrical about 0. We plot c_1 versus a for several values of b in Fig. 8.

There is a prominent dip at $a=1$ when b becomes small. The value of $c_1\to 0$ as $b\to 0$ at $a=1$. At small b, $c_1(a=1,b) = \frac{\sqrt{2}}{3^{1/4}}b^{1/4}(1 - \frac{5}{12\sqrt{3}}b^{1/2} + \cdots)$. This suggests that $\lambda^*_\pm$ will go to zero—or equivalently, the width of the front will diverge—at $a=1$ as $b\to 0$. However, the corrections to $c_1/\sqrt{\mathcal{D}}$ may protect $\lambda^*_\pm$ from reaching zero.

The correction term $c_2/\mathcal{D}$ does improve the match with the exact solution of $\lambda^*_\pm$ as c_1 gets smaller, but this improvement is perturbative—at a given b, it becomes worse with smaller $\mathcal{D}$, so more and more terms in the series are needed. To understand the behavior of λ^*_+ and λ^*_- at $(a=1, b\to 0)$, the following perturbative analysis will be used. We Taylor expand the right-hand side of Eq. (A6) around $a=1$, $b=0$ to first order in b (see the comment about the singular limit in Ref. [27]). For $\lambda<0$, result at arbitrary $\mathcal{D}$ is

$$\frac{ds_1}{d\lambda} = \frac{1}{2\lambda^2}\left[\frac{4b - 6b\mathcal{D}\lambda + 2\mathcal{D}\lambda^3 - 4\mathcal{D}^2\lambda^4 + 2\mathcal{D}^3\lambda^5}{\lambda(1-\lambda\mathcal{D})^2} + O(b^2)\right].$$

We seek a set of λs for which the right-hand side of this equation equals 0. These zeros (or roots) are the zeros of the numerator when the latter do not include 0 and $1/\mathcal{D}$, which is true whenever b is not strictly zero. The negative roots approach 0 as $b\to 0$. As b deviates from 0 slightly, the roots that approach 0 will take place at very small and negative λ, and are given asymptotically by the solution to $4b + 2\mathcal{D}\lambda^3 = 0$. All the other terms become less relevant as b and λ approach 0. The only real solution is

$$\lambda^*_- = -\left(\frac{2b}{\mathcal{D}}\right)^{1/3}. \tag{A9}$$

This analysis did not rely on the largeness of $\mathcal{D}$. As a result, this same solution will appear in the small-$\mathcal{D}$ regime. For positive λ, there is a different approximation to the right hand side of Eq. (A6) at small b (see the comment about the singular limit in Ref. [27]). A similar analysis would lead us to conclude that $\lambda^*_+ \to \frac{2}{3\mathcal{D}}$ for $\mathcal{D}$ comparable to 1 or greater. Both of these conclusions—concerning λ^*_- and λ^*_+—were confirmed by the comparison with the numerically computed extrema of $s_1(\lambda)$ from Eq. (A5); see Fig. 9.

The situation at $a=1$ is summarized as follows, with Fig. 9 serving as a useful reference. For any fixed value of b, there exists a large-enough $\mathcal{D}$ when $\lambda^*_\pm$ is approximated well by $\pm c_1(a=1,b)\mathcal{D}^{-1/2}$; higher-order terms in Eq. (A7) become irrelevant. This expression is asymptotically exact at any b as $\mathcal{D}\to\infty$, but it holds approximately down to a certain crossover value of $\mathcal{D}$. This crossover is a function of b. Whenever $\lambda^*_\pm \sim \mathcal{D}^{-1/2}$, we may refer to this as the "large-$\mathcal{D}$" scaling behavior, and this terminology applies for any a and b (we use the "$\sim$" notation to denote asymptotic behavior).

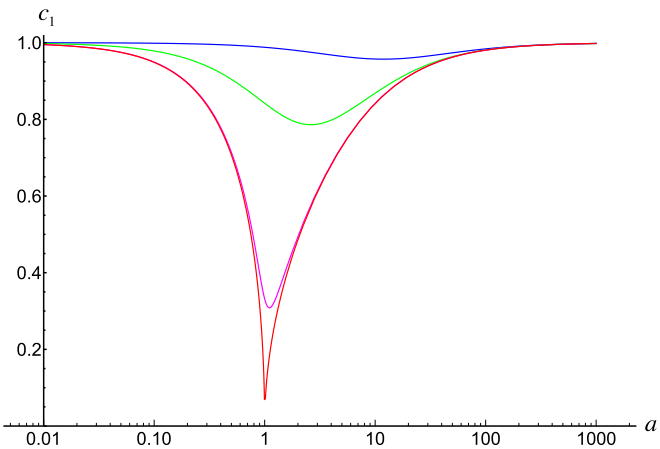

FIG. 8. c_1 versus a for several values of b. From top to bottom: 10 (blue), 1 (green), 10^{-2} (magenta), 10^{-7} (red).

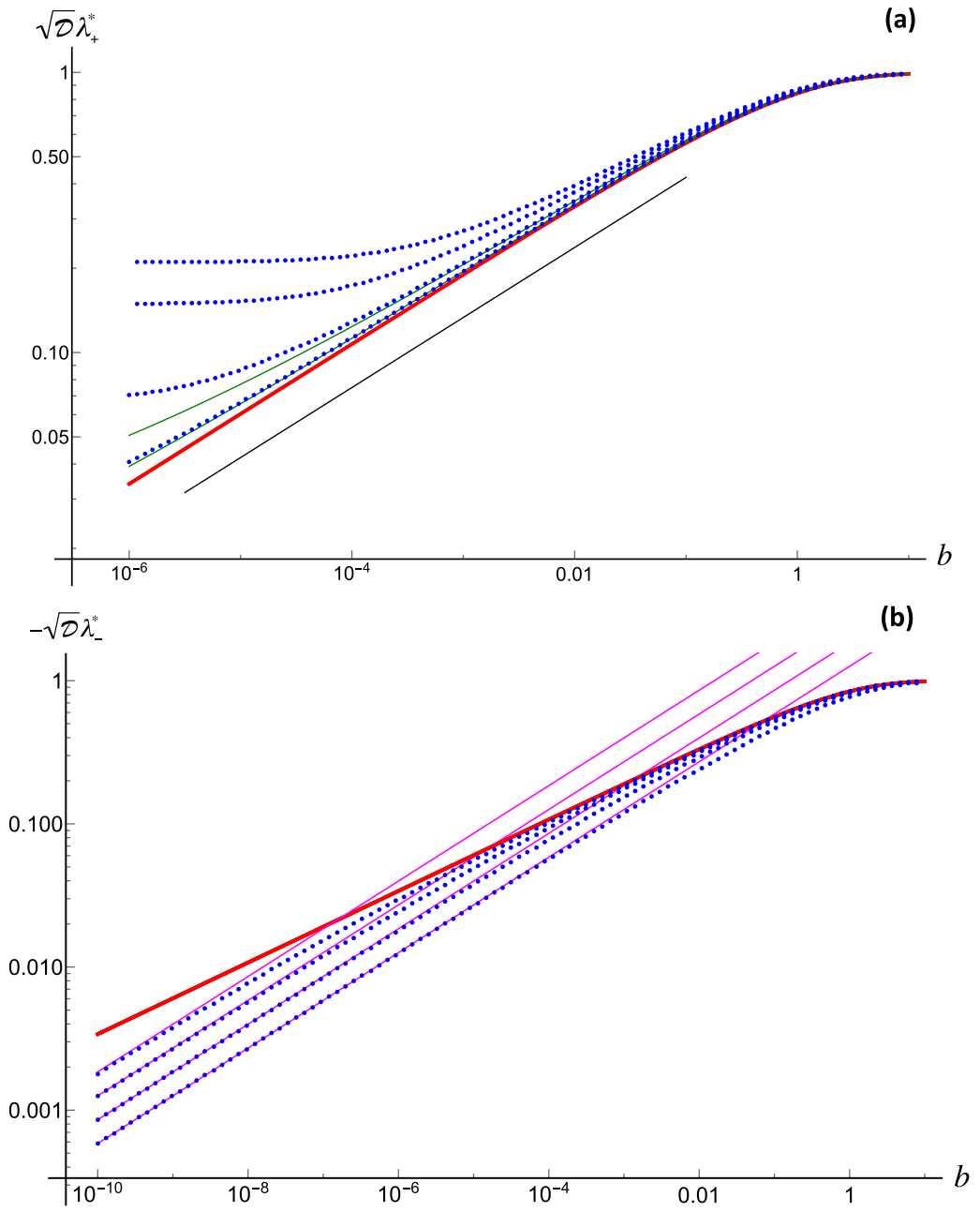

FIG. 9. $\sqrt{\mathcal{D}}\lambda_\pm^*$ versus b at $a = 1$. The dots represent an exact numerical solution to $\lambda_\pm^*$ that satisfy $ds_1/d\lambda = 0$: in panel (a) for $\mathcal{D} = 10$, 20, 100, and 1000, from top to bottom, and in panel (b) for $\mathcal{D} = 1$, 10, 100, and 1000, from bottom to top. The thick red curve represents $\lambda_\pm^*$ from Eq. (A7) with only the first term. It has a small-b asymptotic tail $\frac{\sqrt{2}b^{1/4}}{3^{1/4}}$; the solid black segment has a slope $1/4$ on the log-log scale. The thin green curves in panel (a) represent λ_+^* from Eq. (A7) with the second term included for $\mathcal{D} = 100$, and 1000, indicating that corrections improve the results in the right direction. The magenta lines panel (b) represent the $-(\frac{2b}{\mathcal{D}})^{1/3}$ asymptotic limit to λ_-^* at small b.

Holding $\mathcal{D}$ fixed and decreasing b much below 1, λ_+^* enters the $\sim \frac{\sqrt{2}b^{1/4}}{3^{1/4}}\mathcal{D}^{-1/2}$ asymptotic behavior—as long as $\mathcal{D}$ is bigger than the crossover value at that b. But as b is decreased even further, the $\mathcal{D}^{-1/2}$ scaling eventually breaks down, and λ_+^* crosses over to saturate at $\frac{2}{3\mathcal{D}}$. For $\mathcal{D} \ll 1$, when $\pm c_1(a,b)\mathcal{D}^{-1/2}$ does not apply, λ_+^* also reaches a constant value as $b \to 0$ (see Fig. 9), but it is not given by $\frac{2}{3\mathcal{D}}$. The crossover from $\sim\frac{\sqrt{2}b^{1/4}}{3^{1/4}}\mathcal{D}^{-1/2}$ to $\sim\frac{2}{3}\mathcal{D}^{-1}$ as $b \to 0$ at large $\mathcal{D}$, physically represents an anomalous widening of the front. In contrast, λ_-^* experiences a crossover from $\sim -\frac{\sqrt{2}b^{1/4}}{3^{1/4}}\mathcal{D}^{-1/2}$ to $\sim -(\frac{2b}{\mathcal{D}})^{1/3}$. This represents a true divergence of the front width as $b \to 0$. Because the small-b behavior of λ_-^* is $\sim -(\frac{2b}{\mathcal{D}})^{1/3}$ for any $\mathcal{D}$ (see Fig. 9; the derivation of this formula did not rely on the largeness of $\mathcal{D}$), this divergence of the upwind front as $b \to 0$ at $a = 1$ happens for any $\mathcal{D}$.

On the other hand, holding b fixed and decreasing $\mathcal{D}$ from infinity, leads to a crossover from the large-$\mathcal{D}$ regime with

$\lambda_{\pm}^* \sim \pm c_1(a=1,b)\mathcal{D}^{-1/2}$ to the small-$\mathcal{D}$ regime where this $\mathcal{D}^{-1/2}$ scaling breaks down. If the fixed value of $b \ll 1$, we cross over from $\lambda_{\pm}^* \sim \frac{\sqrt{2}b^{1/4}}{3^{1/4}}\mathcal{D}^{-1/2}$ to $\lambda_{+}^* \sim \frac{2}{3\mathcal{D}}$ or $\lambda_{-}^* \sim -(\frac{2b}{\mathcal{D}})^{1/3}$, and this crossover $\mathcal{D}$ scales as $b^{-1/2}$ for both fronts. We discuss the crossover from the $\mathcal{D}^{-1/2}$ scaling regime as $\mathcal{D}$ is varied at fixed $b \gg 1$ in Appendix A 2 e. In a sense, this is a less interesting crossover regime, because only the point $(a=1,b=0)$ is a critical point—here the crossover is pushed to infinite $\mathcal{D}$, and the upwind front width diverges. As explained in Appendix A 2 e, the crossover point actually goes to zero as $b \to \infty$ for any a.

Thus, as $b \to 0$, the regime when $\lambda_{\pm}^*(\mathcal{D}) \sim \pm\mathcal{D}^{-1/2}$, onsets at larger and larger $\mathcal{D}$. This picture is made especially clear in the middle column of Fig. 11. We note that the phenomenon of the crossover from $\mathcal{D}^{-1/2}$ regime is not unique to $a=1$, but only at $a=1$ the width of the upwind front diverges; when $a \neq 1$, λ_{-}^* and λ_{+}^* reach a constant value as $b \to 0$—front widths do not diverge. This crossover for $a \neq 1$ is discussed in Appendix A 2 e. We discuss implications of this crossover on the behavior of $s_{\pm}^*$ with $\mathcal{D}$ below.

We found a divergent upwind front width for any $\mathcal{D}$ at $a=1$ as $b \to 0$ and an anomalously long downwind front at the same conditions. There are no diverging length scales in the FKPP model at finite $\mathcal{D}$. The diffusion-free model displays nothing pathological at $a=1$, as $b \to 0$ for the downwind front, and has no propagating upwind front for $a=1$ [see Fig. 3(a) in the main text]. Expanding expression for λ_{-}^* from Eq. (5) around $(a=1,b=0)$, we get $-\frac{2b}{a-1}$. So, the upwind front in the $\mathcal{D}=0$ model grows as $b \to 0$ at fixed $a>1$, but it goes to zero as $a \to 1$ at fixed b. Additional insight about diverging front widths comes from the model without advection in the AL, which is studied in Appendix A 3 below. That model predicts both upwind and downwind front widths to diverge at $a=1$ as $\sim b^{-1/4}$; the equivalent of Eq. (A7) has only one term, with no corrections to protect from or change the scaling of divergence of the front width as $b \to 0$.

From all said, it appears that the properties of front widths in the $\mathcal{D}=0$ model around the special point $(a=1,b=0)$ are not related to the case with zero diffusion, but instead are more related to the case with zero advection.

The anomalous growth of the front width is somewhat reminiscent of resonance—with $|a-1|$ akin to detuning, and b akin to damping. At this stage, however, this is only a metaphor.

In returning to the discussion of a general $a \neq 1$, we remind the reader that the expansion in Eq. (A7) is only meant for large $\mathcal{D}$. Therefore, Fig. 8 represents approximations to $|\lambda_{\pm}^*|\sqrt{\mathcal{D}}$ only at large $\mathcal{D}$. As $\mathcal{D}$ is decreased, λ_{+}^* and λ_{-}^* versus a will change, but in different ways. At $\mathcal{D}=1/4$, $\lambda_{+}^* = 1/\sqrt{\mathcal{D}} = 2$ for all a and b. For $\mathcal{D} \ll 1/4$, the plot of λ_{+}^* versus a would resemble the solution to Eq. (5) in the main text up until a certain crossover value of a, when the increase of λ_{+}^* slows down, and eventually saturates at $1/\sqrt{\mathcal{D}}$. This crossover point grows larger with smaller $\mathcal{D}$. Therefore, at any finite a, there is a continuous change in $\lambda_{\pm}^*$ as $\mathcal{D}$ is tuned up from 0.

On the other hand, there is nothing special about λ_{-}^* at $\mathcal{D}=1/4$. Also, the $\mathcal{D}=0$ system has a diverging λ_{-}^* as a approaches 1 from above—see Eq. (5) in the main text (as a reminder, in the $\mathcal{D} \neq 0$ model, the upwind front propagates against advection when $a<1$, whereas it stands still when $\mathcal{D}=0$). At nonzero $\mathcal{D}$, λ_{-}^* stays finite, even at $a=1$. Close to $a=1$, the divergence is replaced by a rapidly growing $|\lambda_{-}^*|$ as a decreases past 1, but this growth slows down at smaller a, and λ_{-}^* eventually saturates at $-1/\sqrt{\mathcal{D}}$ as $a \to 0$. For $a>1$, λ_{-}^* from Eq. (5) in the main text becomes closer and closer to the true λ_{-}^* as $\mathcal{D} \to 0$ up until a certain large crossover value of a. At this point the growth in λ_{-}^* versus a slows down, and it eventually saturates at $-1/\sqrt{\mathcal{D}}$—similar to what happens with λ_{+}^*. Again, this crossover point grows larger with smaller $\mathcal{D}$. We shall examine the small-$\mathcal{D}$ behavior of both fronts below.

When $c_1 \neq 0$, i.e., in the exception of $(a=1,b \to 0)$, we may substitute $\lambda_{\pm}^* = \pm\frac{c_1}{\sqrt{\mathcal{D}}}$ into s_1 from Eq. (A5) and expand the numerator in $\frac{1}{\sqrt{\mathcal{D}}}$. We would obtain:

$$s_{\pm}^* = v_{\text{eff}} \pm 2\sqrt{\mathcal{D}_{\text{eff}}} + O\left(\frac{1}{\sqrt{\mathcal{D}}}\right), \tag{A10}$$

$$\text{where} \quad v_{\text{eff}} = \frac{1}{2} + \frac{-1+a-b-c_1^2}{2\sqrt{-2a+a^2+2ab-2ac_1^2+\left(1+b+c_1^2\right)^2}}, \tag{A11}$$

$$\text{and} \quad \mathcal{D}_{\text{eff}} = \left(\frac{1-a-b+c_1^2+\sqrt{-2a+a^2+2ab-2ac_1^2+\left(1+b+c_1^2\right)^2}}{4c_1}\right)^2 \mathcal{D}, \tag{A12}$$

and c_1 is given in Eq. (A8). The expressions in Eqs. (A11) and (A12) are cumbersome, but we notice from Fig. 8 that sufficiently far from $(a=1,b=0)$, c_1 can be approximated by 1, corresponding to the FKPP $\lambda_{\pm}^*$. This leads to much simpler formulas for $s_{\pm}^*$, quoted in the main text as Eqs. (11) and (12). We plot $\mathcal{D}_{\text{eff}}/\mathcal{D}$ and v_{eff} obtained using both of these methods in Fig. 10.

Figure 11 compares $s_{\pm}^*$ from Eqs. (A11) and (A12) with $s_{\pm}^*$ obtained with the numerically computed extrema of $s_1(\lambda)$ from Eq. (A5). For mathematically typical parameters, i.e., away from the $(a=1,b=0)$ point, such asymptotic theory works remarkably well, even for $\mathcal{D}$ comparable to 1/4. The simpler theory based on setting $c_1=1$ has a larger exclusion region around $(a=1,b=0)$ where it does not perform well.

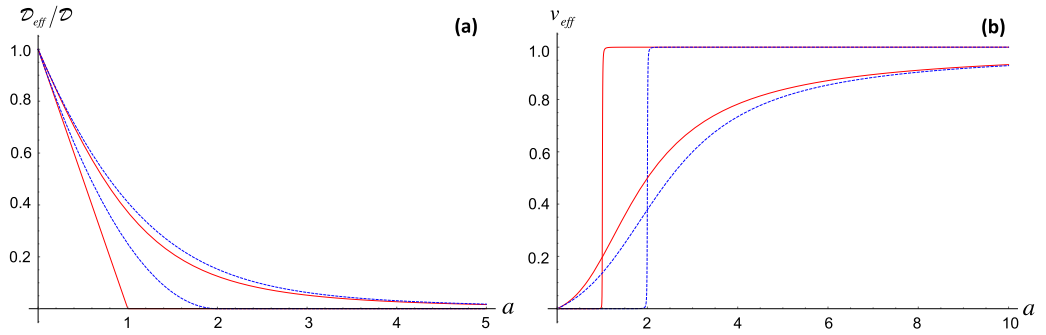

FIG. 10. $\mathcal{D}_{\rm eff}/\mathcal{D}$ vs. a in panel (a) and $v_{\rm eff}$ vs. a in panel (b). We used Eqs. (A11) and (A12) and either c_1 from Eq. (A8) (red, solid curve) or the simpler approximations obtained by setting $c_1 = 1$—which gives Eqs. (11) and (12) in the main text (blue, dashed curves). The results are shown for $b = 10^{-5}$ (bigger discrepancy) and $b = 0.5$ (smaller discrepancy).

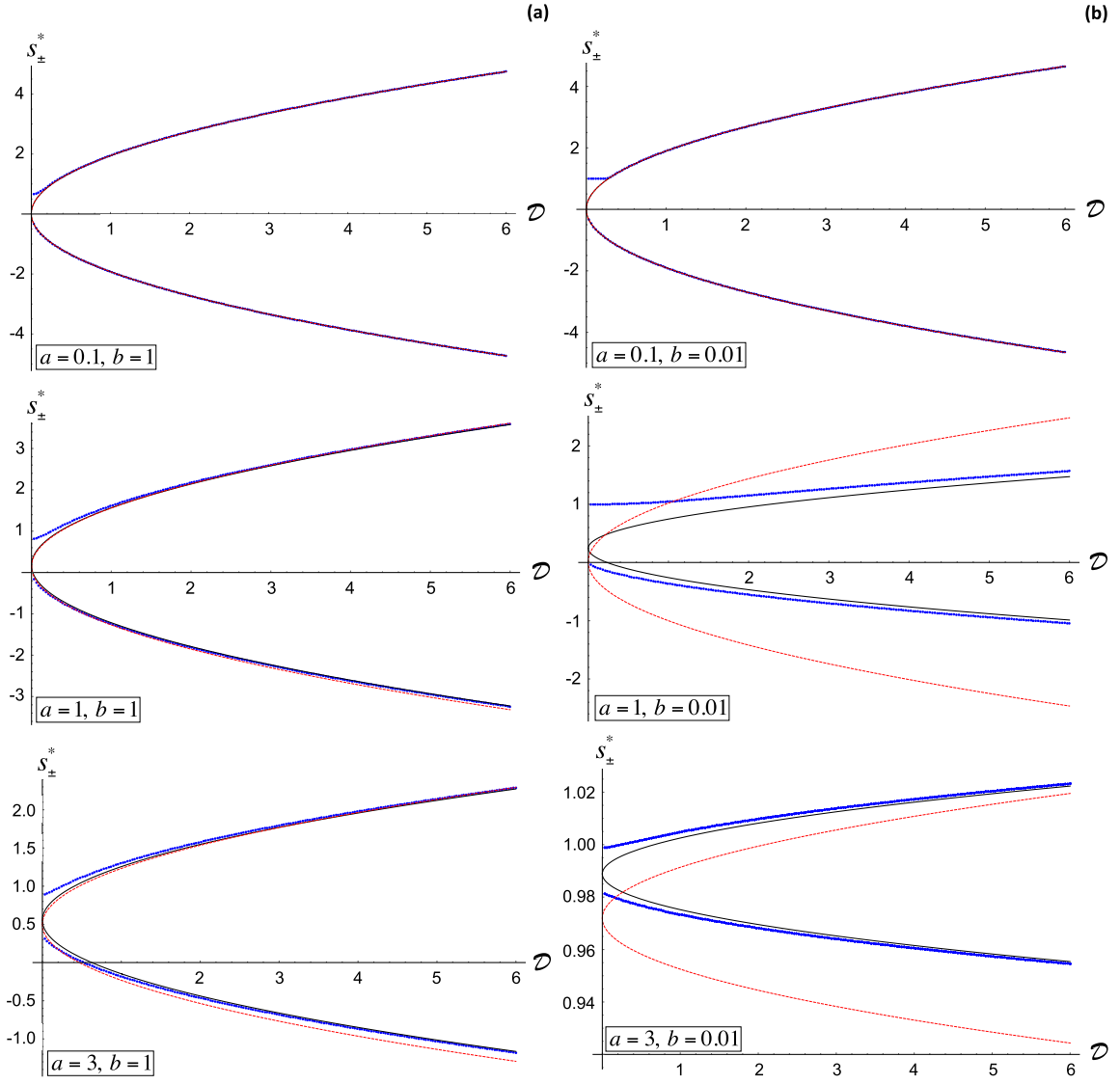

FIG. 11. Comparison of $s^*_\pm$ obtained from the exact minimum of $s_1(\lambda)$ (thick blue dots, closely spaced) with the large-$\mathcal{D}$ asymptotic Eq. (A10), where $v_{\rm eff}$ and $\mathcal{D}_{\rm eff}$ are given, respectively, by Eqs. (A11) and (A12) and using c_1 from Eq. (A8) (solid black) or with simpler approximations obtained by setting $c_1 = 1$, resulting in Eqs. (11) and (12) in the main text (dashed red). With the exception of ($a = 1$, $b = 0.01$), ($a = 3$, $b = 1$), and ($a = 3$, $b = 0.01$), these two analytical approximations are indistinguishable. Also, note the scale on the bottom, right panel. Here the column (a) on the left is for $b = 1$ and column (b) on the right is for $b = 0.01$.

It is important to point out that v_{eff} is the offset of the large-$\mathcal{D}$ asymptotic $s_{\pm}^{*}$, and is not meant to represent $s_{\pm}^{*}$ at $\mathcal{D}=0$, which will be predicted by the $\mathcal{D}=0$ model (see also next section). For example, $s_{\pm}^{*}$ at $\mathcal{D}=0$ will be zero for $a \leqslant 1$.

As expected from the discussion above, the comparison of $s_{\pm}^{*}(\mathcal{D})$ based on the extrema of $s_1(\lambda)$ with the asymptotic theory based only on the first term in Eq. (A7) is worst at $a=1$ as b becomes small. However, at any finite b, the approximation $\lambda_{\pm}^{*} \approx c_1/\sqrt{\mathcal{D}}$, and the resulting expression for $s_{\pm}^{*}$, will always become asymptotically-accurate at sufficiently large $\mathcal{D}$. This was clearly seen in Fig. 9—as $\mathcal{D}$ grows, $\sqrt{D}\lambda_{\pm}^{*} \to c_1(a=1,b)$ at any finite b (and a). On the other hand, as $\mathcal{D}$ is lowered at fixed b, the $\pm c_1/\sqrt{\mathcal{D}}$ behavior of $\lambda_{\pm}^{*}$ ceases to hold. When $b \ll 1$, it crosses over to $\lambda_{+}^{*} \sim \frac{2}{3\mathcal{D}}$ and $\lambda_{-}^{*} \sim -(\frac{2b}{\mathcal{D}})^{1/3}$ (at $a=1$). The crossover away from $a=1$ and small b parameter region is discussed in Appendix A 2 e. In all cases, the speed $s_{\pm}^{*}$ is obtained by substituting $\lambda_{\pm}^{*}$ into Eq. (A5). Additional intuition can be gained from the study of small $\mathcal{D}$ limit, to which we now turn.

b. Small $\mathcal{D}$

The main goal of this subsection is to derive the behavior of $s_{\pm}^{*}$ versus $\mathcal{D}$ as $\mathcal{D} \to 0$, and to show when this behavior is linear in $\mathcal{D}$. The linear behavior will indicate that the FKPP-type of behavior does not extend to zero $\mathcal{D}$. At the end we will synthesize the information from this and the previous subsections to establish the lower limits in $\mathcal{D}$ for the breakdown of the FKPP-type behavior.

When $\mathcal{D}=0$, Eq. (A5) turns into Eq. (A4). The appearance of new $\mathcal{D}$-terms in Eq. (A5) does not change the positions of extrema discontinuously—if they take place at finite values in the $\mathcal{D}=0$ problem (the smaller is the $\mathcal{D}$, the larger the λ should be in order for the effect of new terms to take place).

This is true for λ_{+}^{*}, so we can study its change due to the appearance of diffusion perturbatively—by tracking the change in the position of λ_{+}^{*}. We follow the following procedure. First, substitute the ansatz [see Eq. (5) in the main text],

$$\lambda_{+}^{*} = \frac{1+a+b+2\sqrt{a}}{1+\sqrt{a}} + c\mathcal{D},$$

into Eq. (A6), and Taylor-expand the resulting expression to linear order in $\mathcal{D}$, giving an expression of the form $A\mathcal{D}$ (as expected, there is no $\mathcal{D}^0$ term). Next, we solve for c that makes this A zero. The result is

$$c = \frac{(1+a+b+2\sqrt{a})^2}{(1+\sqrt{a})^2}\frac{(2+(3-a-b)\sqrt{a})}{2(1+\sqrt{a})^2}.$$

We then substitute the ansatz for λ_{+}^{*} with this c into Eq. (A5) and again expand in $\mathcal{D}$ to first order. We get

$$s_{+}^{*} = \left(1+\frac{b}{(1+\sqrt{a})^2}\right)^{-1} + \left(\frac{b}{\sqrt{a}+1}\right)\mathcal{D} + \cdots \quad \text{(A13)}$$

The first term unsurprisingly matches s_{+}^{*} from the $\mathcal{D}=0$ model [see Eq. (4) in the main text]. The correction is the quantity we seek—the slope of s_{+}^{*} versus $\mathcal{D}$—see Fig. 4(a) in the main text. This demonstrates that unless b goes to infinity—when particles spend essentially all of the time on the GL—s_{+}^{*} scales like an integer power of $\mathcal{D}$ instead of the $\sqrt{\mathcal{D}}$ scaling from the FKPP model.

With λ_{-}^{*}, the situation is less straightforward, as the position of the maximum at negative λ moves to $-\infty$ as $a \to 1$ from above when $\mathcal{D}=0$. So the approach by tracking the maximum of $s_1(\lambda)$ (for $\lambda<0$) as $\mathcal{D}$ is turned up from zero while a crosses 1 (see Figs. 5–7) will not work—there is no maximum in the $\mathcal{D}=0$ problem for $a<1$, whereas it exists in the $\mathcal{D}\neq 0$ system. Instead, we Taylor-expand the right-hand side of Eq. (A6) in $\mathcal{D}$ around 0 and find the leading-order asymptotic expression at large negative λ. The magnitude of λ has to be large, because that is where the zeros are located at small $\mathcal{D}$ and a close to 1. The resulting equation for λ_{-}^{*} is a simple cubic:

$$0 = (a-1) + \frac{2ab}{\lambda} + \lambda^2\mathcal{D}. \quad \text{(A14)}$$

Negative λ that satisfies Eq. (A14) is the λ_{-}^{*} we seek. Note that the first term merely offsets the function in the y direction, so the solution for λ is a smooth function of a. When $a=1$, the solution is simple: $\lambda_{-}^{*} = -(\frac{2b}{\mathcal{D}})^{1/3}$. We have already seen this very formula in the discussion of the large-$\mathcal{D}$ regime. We have argued that this asymptotic is valid below a crossover which separates this small-$\mathcal{D}$ regime and the large-$\mathcal{D}$ regime when $\lambda_{-}^{*} \sim -c_1(a=1,b)\mathcal{D}^{-1/2}$ (and that this crossover $\sim b^{-1/2}$ for $b \ll 1$). To get s_{-}^{*} in this regime, we substitute this into Eq. (A5), which gives a rather cumbersome expression. An expansion in $\mathcal{D}^{1/3}$ has the following leading-order term:

$$s_{-}^{*}(a=1) = -\frac{3b^{1/3}\mathcal{D}^{2/3}}{2^{2/3}}. \quad \text{(A15)}$$

The result in Eq. (A15) was confirmed by the comparison with the numerically obtained maximum of the exact $s_1(\lambda)$ for $\lambda<0$. This numerical solution also confirmed $\lambda_{-}^{*} = -(\frac{2b}{\mathcal{D}})^{1/3}$. Echoing our findings at large $\mathcal{D}$, the upwind front width diverges as $b \to 0$ at $a=1$. This is not so for λ_{+}^{*} (see above).

We also see from Eq. (A14) that when $\mathcal{D}=0$, $\lambda_{-}^{*} = \frac{-2b}{a-1} + \cdots$. This is in fact the leading-order term in the expansion of $\lambda_{-}^{*}(\mathcal{D}=0) = \frac{1+a+b-2\sqrt{a}}{1-\sqrt{a}}$ (see Eq. (5) in the main text) around $a=1$.

Next, we are going to set $\epsilon = a-1$ in the first term of Eq. (A14), and approximate a by 1 in the second term [Eq. (A14) is not exact—it is a consequence of a low-order expansion, so keeping higher order terms in subsequent calculations is pointless]. Thus, we seek a solution to

$$\epsilon + \frac{2b}{\lambda} + \lambda^2\mathcal{D} = 0.$$

From the structure of the function of λ on the left-hand side, and the fact that b and $\mathcal{D}$ are always positive, we see that there can be at most one negative root. It helps to rewrite this in a standard form for a cubic equation,

$$\lambda^3 + \left(\frac{\epsilon}{\mathcal{D}}\right)\lambda + \left(\frac{2b}{\mathcal{D}}\right) = 0. \quad \text{(A16)}$$

The solution for positive ϵ is

$$\left(\frac{b}{\mathcal{D}}\right)^{1/3}\left\{\left[-1+\sqrt{1+\left(\frac{\epsilon}{3b^{2/3}\mathcal{D}^{1/3}}\right)^3}\right]^{1/3} - \frac{\left(\frac{\epsilon}{3b^{2/3}\mathcal{D}^{1/3}}\right)}{\left[-1+\sqrt{1+\left(\frac{\epsilon}{3b^{2/3}\mathcal{D}^{1/3}}\right)^3}\right]^{1/3}}\right\}, \tag{A17}$$

which is real and negative over that domain, so it is indeed λ_-^* when $\epsilon > 0$. We are working in the neighborhood of small ϵ and $\mathcal{D}$. Evidently, $\frac{\epsilon}{3b^{2/3}\mathcal{D}^{1/3}}$ is a natural measure of prevalence of each of these parameters. One can easily show that when $\mathcal{D} \ll \frac{\epsilon^3}{27b^2}$, λ_-^* saturates to $-\frac{2b}{\epsilon}$, and when $\mathcal{D} \gg \frac{\epsilon^3}{27b^2}$, $\lambda_-^* \sim -(\frac{2b}{\mathcal{D}})^{1/3}$. These two limits match the expressions that we have just discussed separately. As $\mathcal{D}$ is increased further, the $-(\frac{2b}{\mathcal{D}})^{1/3}$ behavior of λ_-^* eventually meets a second crossover and gives way to the $\sim c_1(1+\epsilon,b)\mathcal{D}^{-1/2}$ asymptotic behavior. We have shown that the function $c_1(a,b)$ goes to a finite value as $b \to 0$ when $a \neq 1$, so this suggests that both crossovers continues to increase, in contradiction to the expectation that $\lambda_\pm^* \sim \mathcal{D}^{-1/2}$ at large-enough $\mathcal{D}$ when $a \neq 1$ (see the previous subsection on Large $\mathcal{D}$). However, the calculations here are based on an expansion around $\mathcal{D} = 0$, and will break down at large-enough $\mathcal{D}$. Thus, in practice—as verified by the numerical calculations of Eq. (A6)—the crossover to the $\sqrt{\mathcal{D}}$ scaling behavior does not continue to increase as b is lowered, if $\epsilon \neq 0$.

It is also worth mentioning that empirically, the expression in Eq. (A17) is well approximated by $-[(\frac{\epsilon}{2b})^2 + (\frac{\mathcal{D}}{2b})^{2/3}]^{-1/2}$. The expression [...] appearing in Eq. (A17) is not real and negative for $\epsilon < 0$, so will need to choose another solution there; the two solutions must join in a continuous fashion, since as already mentioned, λ_-^* changes smoothly as ϵ crosses zero. We first study the positive ϵ case.

As was the case with λ_-^*, we are interested in the functional behavior of s_-^* versus very small $\mathcal{D}$, primarily to demonstrate that a correction to s_-^* at $\mathcal{D} = 0$ is proportional to an integer power of $\mathcal{D}$, and therefore, strongly departs from any FKPP-like predictions. To do this, we expand the [...] quantity in Eq. (A17) to the first two terms in small $\frac{\epsilon}{3b^{2/3}\mathcal{D}^{1/3}}$, and get

$$\lambda_-^* = -\frac{2b}{\epsilon}\left(1 - \frac{4b^2\mathcal{D}}{\epsilon^3}\right). \tag{A18}$$

The leading-order term is $-\frac{2b}{\epsilon}$ as can be seen. When this expression is substituted into Eq. (A5), and the result is expanded in ϵ and $\mathcal{D}$, we get $s_-^* = [\frac{\epsilon^2}{4b} + O(\epsilon^3)] - [\frac{2b}{\epsilon} + O(\epsilon^0)]\mathcal{D}$. The calculation presented in this subsection was based on an expansion in $\epsilon = a - 1$ and $\mathcal{D}$. Therefore, we cannot hope to capture the $\mathcal{D}^0$ term fully. Now, s_1 in Eq. (A5) upon which this perturbative analysis is based, reduces when $\mathcal{D} = 0$, to s_1 in Eq. (A4) for which $s_-^* = (1 + \frac{b}{(1-\sqrt{1+\epsilon})^2})^{-1}$ [Eq. (4) in the main text]. Moreover, the leading term in the ϵ-expansion of this quantity is indeed $\frac{\epsilon^2}{4b}$ (the cubic terms also agree).

The slope $-\frac{2b}{a-1}$ in the expression for s_-^* versus $\mathcal{D}$ was derived with the assumption that $a - 1 > 0$ is small. Had we used the procedure used for λ_+^* [Eq. (A13)], we would find that the slope is $-\frac{b}{\sqrt{a}-1}$, which does not rely on the smallness $a - 1$. However, the two results become equivalent when $a - 1 \ll 1$. Therefore, we can conclude that

$$s_-^* = \left(1 + \frac{b}{(1-\sqrt{a})^2}\right)^{-1} - \left(\frac{b}{\sqrt{a}-1}\right)\mathcal{D} + \cdots \tag{A19}$$

This result agrees with s_-^* computed numerically from the exact maximum of $s_1(\lambda)$ from Eq. (A5) for $\lambda < 0$. The $\mathcal{D}$-correction is the quantity we seek—the slope of s_-^* versus $\mathcal{D}$ at zero $\mathcal{D}$. This slope goes to infinity as $\epsilon \to 0$, since at $\epsilon = 0$, $s_-^* \sim -\mathcal{D}^{1/3}$, which has an infinite slope at zero $\mathcal{D}$.

We now address the negative ϵ case (i.e., $a < 1$). In this domain of ϵ, the following is the root of Eq. (A16) that is real and negative:

$$\left(\frac{b}{\mathcal{D}}\right)^{1/3}\left\{(-1)^{2/3}\left[-1+\sqrt{1+\left(\frac{\epsilon}{3b^{2/3}\mathcal{D}^{1/3}}\right)^3}\right]^{1/3} + \frac{(-1)^{1/3}\left(\frac{\epsilon}{3b^{2/3}\mathcal{D}^{1/3}}\right)}{\left[-1+\sqrt{1+\left(\frac{\epsilon}{3b^{2/3}\mathcal{D}^{1/3}}\right)^3}\right]^{1/3}}\right\}. \tag{A20}$$

One can show that when $\mathcal{D} \ll \frac{\epsilon^3}{27b^2}$, $\lambda_-^* \sim \frac{\sqrt{-\epsilon}}{\mathcal{D}^{1/2}}$, and when $\mathcal{D} \gg \frac{\epsilon^3}{27b^2}$, $\lambda_-^* \sim -(\frac{2b}{\mathcal{D}})^{1/3}$ as before. Again, at larger $\mathcal{D}$ there is a second crossover to the $\sim c_1(1+\epsilon,b)\mathcal{D}^{-1/2}$ asymptotic behavior. The position of the first crossover scales like ϵ^3, and at $\epsilon = 0$, the $(\frac{2b}{\mathcal{D}})^{1/3}$ asymptotic extends all the way to $\mathcal{D} = 0$. Interestingly, there is a $\mathcal{D}^{-1/2}$ scaling on both sides of the $\mathcal{D}^{-1/3}$ scaling, which disappears altogether with large-enough ϵ, when the two crossovers meet. In $\mathcal{D} \ll \frac{\epsilon^3}{27b^2}$ regime—the very first scaling behavior around $\mathcal{D} = 0$ before the first crossover—the speed will behave as $s_-^* \sim -2\sqrt{1-a}\sqrt{\mathcal{D}}$. This result also agrees with the low $-\mathcal{D}$ tail of s_-^* computed numerically from the exact maximum of $s_1(\lambda)$ from Eq. (A5) for $a < 1$.

If, instead of b being fixed, it was some given fraction of a, i.e., $b = ra = r(1+\epsilon)$ (for example, $r = 1$ in Fig. 4 in the main text), all of the above results for λ_-^* and s_-^* that are given as series in ϵ (or $a - 1$) would hold at the leading-order in ϵ by replacing $b \to r$.

c. *Stalling condition for the upwind front*

Equation (A19) lets us derive $\mathcal{D}_{\text{stall}}$. We can see that for $a - 1 > 0$,

$$\mathcal{D}_{\text{stall}} \approx \frac{(a-1)^3}{8b^2}. \tag{A21}$$

As a increases, the position of $\mathcal{D}_{\text{stall}}$ also increases. Eventually, it enters the regime where large-$\mathcal{D}$ theory should apply, so $\mathcal{D}_{\text{stall}}$ will come from the condition $v_{\text{eff}} = 2\sqrt{\mathcal{D}_{\text{eff}}}$ (recall that $\mathcal{D}_{\text{eff}}$ is proportional to $\mathcal{D}$). Using the simpler formulas, Eqs. (11) and (12) from the main text, we predict

$$\mathcal{D}_{\text{stall}} = \frac{\left[1 + \frac{a-b-2}{\sqrt{a^2+2a(b-2)+(b+2)^2}}\right]^2}{[2-a-b+\sqrt{a^2+2a(b-2)+(b+2)^2}]^2}. \tag{A22}$$

This agrees well with $\mathcal{D}_{\text{stall}}$ obtained from the more exact Eqs. (A11) and (A12), except for b very close to 0 and a close to 1 (although, the latter is also an approximation that works worst in these conditions). At large a and b, both results have the following leading-order behavior:

$$\mathcal{D}_{\text{stall}} = \left(\frac{a}{2b}\right)^2. \tag{A23}$$

This shows that when a and b are both varied in such a way so as to keep their ratio constant, $\mathcal{D}_{\text{stall}}$ will have this limiting value. For example, when $a = b$, $\mathcal{D}_{\text{stall}}$ will approach 1/4 that we see in Fig. 4(b) in the main text.

d. Common intersection point at $\mathcal{D} = 1/4$

When $\mathcal{D} = 1/4$, $\lambda_+^* = 2$ solves Eq. (A6) for any a and b. Substituting these values into Eq. (A5) gives the speed of 1, for any a and b. More details can be found in our "Large-$\mathcal{D}$" discussion.

e. Crossover into the $\sqrt{\mathcal{D}}$ behavior

We have discussed this crossover at length for $a = 1$, but not for general parameters. This crossover is important because it addresses the question under what conditions the behavior of the model becomes FKPP-like. This is a challenging topic, because a crossover can be defined in multiple ways, each predicting a somewhat different crossover $\mathcal{D}$. Moreover, in addition to the characteristic position of the crossover itself, the width of the crossover region is an additional quantity that characterizes crossover physics. The following discussion will consider crossovers in different regions of (a,b) space, from which an overall picture should emerge. We will show that the crossover surface, as a function of a and b, is complicated—reflecting the richness of the phenomenology that arises when advection and diffusion are in competition—something that does not happen in a basic reaction-diffusion model with an advective term.

We first discuss the downwind front. In the limit of both a and $b \to 0$, there is a sharp crossover at $\mathcal{D} = 1/4$, such that $s_+^* \to 1$ for $\mathcal{D} < 1/4$ and $s^* \to 2\sqrt{\mathcal{D}}$ for $\mathcal{D} > 1/4$ as both $a \to 0$ and $b \to 0$. As stated in the main text, the word sharp refers to the smallness of the width of the crossover region—thus, the asymptotics on both sides remain valid right up to the crossover point; it does not refer to the discontinuity of derivatives, although in this particular case of a, $b \to 0$ the derivative of $s_+^*(\mathcal{D})$ is indeed discontinuous at $\mathcal{D} = 1/4$. To see the existence of a sharp crossover at $\mathcal{D} = 1/4$, note that when $a = 0$ and $b = 0$, Eq. (A3) predicts two branches: $s = 1$ and $s = 1/\lambda + \mathcal{D}\lambda$. The minimum value of the latter is $2\sqrt{D}$. These two branches will intersect for $\mathcal{D} < 1/4$, and the intersection points take place at $\lambda = (1 \pm \sqrt{1-4\mathcal{D}})/2\mathcal{D}$. On the other hand, as $a \to 0$, $b \to 0$, the choice of branches is such that in between these two intersection points, s_1 is given by 1, and otherwise, it is given by $1/\lambda + \mathcal{D}\lambda$. The key to these calculations is the remark about singular limits in Ref. [27]. Making a and b nonzero will create a gap between the branches $s_1(\lambda)$ and $s_2(\lambda)$, but as $a,b \to 0$, the gap is very small, so $s_+^* \approx 1$ for $\mathcal{D} < 1/4$ (recall, that the selected speed for the downwind front takes place at the minimum value of the top branch). Therefore, as both a and $b \to 0$, $s_+^* \approx 1$ for $\mathcal{D} < 1/4$, and $s_+^* \approx 2\sqrt{\mathcal{D}}$ for $\mathcal{D} > 1/4$, i.e., the crossover to the $\sqrt{\mathcal{D}}$ behavior is very sharp, and takes place at $\mathcal{D} = 1/4$. This is the regime when the mechanism that gives the biggest speed dominates. By a similar argument, when only $a \to 0$, the crossover will take place at $\mathcal{D} = [4(1+b)]^{-1}$. For $\mathcal{D}$ somewhat below this value,

$$s_+^* \approx 1 - \frac{2b\mathcal{D}}{1 - \sqrt{1 - 4\mathcal{D}(1+b)}}, \tag{A24}$$

while for $\mathcal{D}$ somewhat above this value, $s_+^* \approx 2\sqrt{\mathcal{D}}$—the FKPP result. Also, for $\mathcal{D}$ somewhat below this value,

$$\lambda_+^* \approx \frac{1 - \sqrt{1 - 4\mathcal{D}(1+b)}}{2\mathcal{D}}, \tag{A25}$$

while for $\mathcal{D}$ somewhat above this value, $\lambda_+^* \approx \frac{1}{\sqrt{\mathcal{D}}}$—the FKPP result. Note that as b is also made small, the prediction of Eq. (A24) goes to 1, the result discussed above, and the prediction of Eq. (A25) goes to $(1 - \sqrt{1-4\mathcal{D}})/(2\mathcal{D})$. The transition between these behaviors takes place in a very narrow region of $\mathcal{D}$; i.e., it is also a sharp crossover. The width of the transition region goes to zero as $a \to 0$. As b increases, there is a greater tendency for the GL to dominate—particles spend less and less time in the AL, and we expect the crossover to shift to lower and lower $\mathcal{D}$. We will examine the regime of large b below.

Another approach to estimating the crossover is by examining the intersection of the small-$\mathcal{D}$ limit given by $s_\pm^* = \frac{1}{1+\frac{b}{(1\pm\sqrt{a})^2}} \pm \frac{b\mathcal{D}}{\sqrt{a}\pm 1}$ (see Appendix A 2 b, where this result is derived; note that at $a = 0$, these are the first two terms in the $\mathcal{D}$-Taylor expansion of s_+^* from the previous paragraph) with the large-$\mathcal{D}$ limit $v_{\text{eff}} \pm 2\sqrt{\mathcal{D}_{\text{eff}}}$, where the parameter dependence for $\mathcal{D}_{\text{eff}}$ and v_{eff} given by Eqs. (A11) and (A12). For example, recall that in the large-$\mathcal{D}$ asymptotic, $\mathcal{D}_{\text{eff}} \to \mathcal{D}$ and $v_{\text{eff}} \to 0$ as $a \to 0$ for any b (see also Fig. 10). Such asymptotic matching argument also suggests a sharp crossover for small a and b, as well as the lowering of the crossover point as b grows. This method of estimating the crossover may fail for b somewhat above a certain value that depends on a, since these two asymptotics may not actually intersect. However, it can be used to gain a qualitative understanding of how the crossover varies with parameters in the neighborhood of the $(a,b) = (0,0)$ corner. This is shown in Fig. 12.

Taking this alternative definition of a crossover, and letting $a \to 0$, will not produce the identical result as the first definition—it will lie somewhat below $[4(1+b)]^{-1}$. The prediction based on Eq. (A24) is more accurate, because this result was obtained by a nonperturbative method that gives an exact $a_+^*(\mathcal{D})$ for $\mathcal{D}$ all the way up to the crossover value in the limit of $a \to 0$. But, whereas the previous definition will work very well for $a \ll 1$, the current definition can be extended to values larger than 1.

When $a \gg 1$, the slope of $s_+^*(\mathcal{D})$ at $\mathcal{D} = 0$ is small when $b \ll \sqrt{a}$. In this regime, $\mathcal{D}_{\text{eff}} \to 0$ and $v_{\text{eff}} \to 1$. A log-log plot of the numerically obtained s_+^* reveals that the crossover moves to lower $\mathcal{D}$ as a increases. However, this crossover is not very meaningful, because s_+^* grows very slowly (note that $\mathcal{D}_{\text{eff}}$ decreases with increasing a), and remains ≈ 1 until a very large $\mathcal{D}$ [see inset in Fig. 4(a) in the main text]. As b

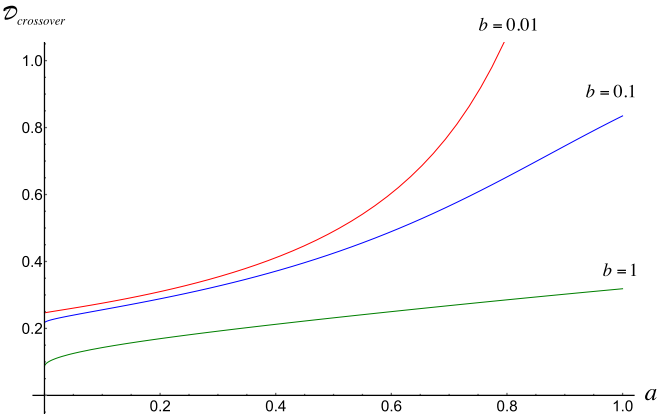

FIG. 12. Crossover defined from the intersection of $\frac{1}{1+\frac{b}{(1\pm\sqrt{a})^2}} \pm \frac{b\mathcal{D}}{\sqrt{a}\pm 1}$ and $v_{\rm eff} \pm 2\sqrt{\mathcal{D}_{\rm eff}}$.

increases, eventually becoming $\gg \sqrt{a}$, the crossover moves to an even smaller value of $\mathcal{D}$, as expected physically.

In summary, the crossover $\mathcal{D}$ into the FKPP regime for the downwind front $\to 1/4$ when both a and $b \to 0$. Moving away from this corner in parameter space, the crossover will decrease with increasing b and increase with increasing a below 1, following by a decrease again as a is above 1, but when a is $\gg 1$, increasing a at fixed b leads to s_+^* that is essentially 1 until a very large $\mathcal{D}$. When b increases at fixed a, or at covarying a while their ratio a/b is fixed, the crossover decreases as b^{-2} for large b (see below). As discussed in the previous section, the crossover diverges at $a = 1$ as $b \to 0$—indicating an extreme departure from the FKPP behavior. When both a and b grow much beyond 1, the crossover decreases. Evidently, the crossover surface is quite complicated. The breaking of the Gallilean invariance due to addition of a separate competing transport channel breaks the applicability of a reaction-diffusion picture of front propagation in a nontrivial way.

We briefly discuss the upwind front. As stated above, when $a < 1$, the diffusive mechanism is essential for propagating the front. Therefore, with the exception of a small region of (a,b) parameter space, s_-^* will scale as $-\sqrt{\mathcal{D}}$ when $a < 1$. For $a \gg 1$, all of the downwind front conclusions hold—we know this from the numerical study of s_-^*, the asymptotic matching argument and the large-b analysis that we will now describe.

The following large-b approximation holds for any a, including $a = 1$. As $b \to \infty$, both $\lambda_\pm^*$ and $s_\pm^*$ approach FKPP values. Letting $b = 1/\epsilon$, $\lambda_\pm^* = \frac{\pm 1}{\sqrt{\mathcal{D}}} + c'\epsilon^2$, substituting into Eq. (A6) for s_1 and expanding in ϵ, we obtain

$$\left(8a + \frac{2a}{\mathcal{D}} \pm \frac{8a}{\sqrt{\mathcal{D}}} \pm 4c'\sqrt{\mathcal{D}}\right)\epsilon^2 = 0.$$

We solve for c' and have

$$\lambda_\pm^* = \pm\frac{1}{\sqrt{\mathcal{D}}} \mp \frac{a(1 \mp 4\sqrt{\mathcal{D}} + 4\mathcal{D})}{2b^2\mathcal{D}^{3/2}} \tag{A26}$$

[if instead we guessed that a correction term is $O(1/b)$, the resulting c' will have to be 0]. As $b \to \infty$ at fixed $\mathcal{D}$, the FKPP result dominates. The second term in Eq. (A26) is a correction valid at finite, but large b. As b is further decreased, this result begins to break down. Equating the two terms suggests that at a given $\mathcal{D}$, the correction becomes important when b is

$$b = \sqrt{2a\left(1 \mp \frac{1}{\sqrt{4\mathcal{D}}}\right)^2}.$$

So, at a fixed $\mathcal{D}$, there exists a characteristic b below which the FKPP scaling of $\lambda_\pm^*$ begins to break down. For $\mathcal{D} \ll 1/4$, this crossover b scales like $\mathcal{D}^{-1/2}$. Equivalently, holding the value of b fixed, there is a crossover value of $\mathcal{D}$, below which the FKPP scaling begins to break down. This crossover $\mathcal{D}$ scales like b^{-2} at large b and $\mathcal{D} \ll 1/4$.

Substituting Eq. (A26) into Eq. (A5), and Taylor-expanding in $1/b$ we find

$$s_\pm^* = \pm\sqrt{\mathcal{D}} + \frac{a \mp 2a\sqrt{\mathcal{D}}}{b}. \tag{A27}$$

Again, for the FKPP result to start to break down at a given a and $\mathcal{D} \ll 1/4$, b has to scale as $\mathcal{D}^{-1/2}$.

A similar procedure with $a = rb$, $b \gg 1$ and constant r, will give

$$s_\pm^* = \frac{r}{1+r} \pm \frac{2\sqrt{\mathcal{D}}}{1+r}. \tag{A28}$$

This will hold for all $\mathcal{D}$ as $b \to \infty$.

3. A model without advection

In order to clarify the origin of the richness of the phenomenology discovered above, including diverging front widths and complex crossover phenomenology, we chose to consider a model that has two layers, but does not have advection in the AL. This will turn out to be a very insightful exercise. Thus, we start with the equivalent of Eqs. (A1) and (A2), which now reads

$$-s\frac{d\tilde{\rho}}{dz} = -b\tilde{\rho} + b\tilde{\sigma}, \tag{A29}$$

$$-s\frac{d\tilde{\sigma}}{dz} = f(\tilde{\sigma}) - a\tilde{\sigma} + a\tilde{\rho} + \mathcal{D}\frac{d^2\tilde{\sigma}}{dz^2}. \tag{A30}$$

Then, the equivalent of Eq. (A3) becomes

$$s\lambda = (1-a) + \frac{ab}{b+s\lambda} + \mathcal{D}\lambda^2. \tag{A31}$$

From this, the equivalent of Eq. (A5) is

$$s_{1,2}(\lambda) = \frac{1-a-b+\mathcal{D}\lambda^2 \pm \sqrt{a^2+2a(b-\mathcal{D}\lambda^2-1)+(b+\mathcal{D}\lambda^2+1)^2}}{2\lambda}. \tag{A32}$$

Now, s_1 is the relevant branch, as before. We notice that if we now define $\mu = \lambda\sqrt{\mathcal{D}}$, we have

$$s_1(\lambda) = \frac{1-a-b+\mu^2+\sqrt{a^2+2a(b-\mu^2-1)+(b+\mu^2+1)^2}}{2\mu}\sqrt{D}. \tag{A33}$$

This means that all the extremum points of $s_{1,2}$, are functions of only a and b, or

$$\lambda_{\pm}^{*} = \frac{\mu_{\pm}^{*}(a,b)}{\sqrt{\mathcal{D}}}, \tag{A34}$$

where μ_{+}^{*} refers to μ that minimizes $s_1(\mu)$ for $\mu > 0$ and μ_{-}^{*} refers to μ that maximizes $s_1(\mu)$ for $\mu < 0$. So we learn three very important facts. First, $\lambda_{\pm}^{*}$ are no longer given as a series in powers of $\frac{1}{\sqrt{\mathcal{D}}}$, but there is only one term, where $\mu_{\pm}^{*}$ can be found exactly. Second, $s_{\pm}^{*} \propto \sqrt{\mathcal{D}}$ for all $\mathcal{D}$, and therefore, there will not be the complicated crossover phenomenon. Third, this also indicates that there will be no fragility phenomena either, which is expected, since there is no alternative "transport channel" that competes with the diffusive transport channel.

We can find $\mu_{\pm}^{*}(a,b)$ in a straightforward way by taking the derivative of s_1 with respect to μ and solving for its zeros. The result will consist of complicated expressions. There are two real μ's, which are symmetric about zero. The important finding is that there will also be a dip at $a = 1$, and this dip goes to zero as $b \to 0$. At small b, $\mu(a = 1,b) \sim \frac{\sqrt{2}}{3^{1/4}} b^{1/4}$. Now this asymptotic expression is valid to arbitrarily small nonzero b—there will not be a crossover to a different scaling or to a constant value as it happened in the presence of advection.

There is another way to view the absence of fragility in the advection-free model. Consider the advective model in the original variables. At fixed v_0 and small D, the downwind speed will be given approximately by $s_{+}^{*} = \frac{v_0}{1+\frac{\beta}{(\sqrt{\delta}+\sqrt{\alpha})^2}}$. In contrast, the FKPP speed is given by $2\sqrt{\delta D}$. Thus, an infinitesimal coupling the FKPP model to the AL will cause a finite change in the speed, indicating fragility. However, the magnitude of this finite change decreases with v_0, and when v_0 becomes zero, the coupling of the FKPP model to the AL—which now acts as a storage only layer—ceases to cause fragility.

4. Numerical investigation of the validity of the UTF assumption for $\mathcal{D} \neq 0$ case

Our derivation of the front speed and decay or growth rate of the front in the zero diffusion case does not have to rely on the UTF assumption—only the pulled nature of the front. For instance, the derivation of those results presented in the main text uses a direct solution described in the next section, Appendix B, and does not invoke a UTF assumption; there is also an alternative method discussed in Appendix C. Nevertheless, we do address the validity of UTF profiles briefly in discussing the numerical method in Appendix E 3.

On the other hand, when dealing with a $\mathcal{D} \neq 0$ case, we did assume that $\rho(x,t) = \rho(x - st)$ and $\sigma(x,t) = \sigma(x - st)$, and used the ideas from the theory of pulled fronts to extract the speed—which matches front speeds from the numerical solutions of (the dimensionless version of) Eqs. (1) and (2) with a logistic growth model. To further verify the validity of a UTF ansatz we plot, in Figs. 13–15, front shapes obtained from the numerical solution of these equations at two different times. The shapes of fronts remain virtually identical, so within the precision of our numerical method, the stationarity of front shapes appears justified.

The parameter values used in these figures were chosen because they sample different types of dynamical behaviors found. These are: the counter-wind motion of the upwind front

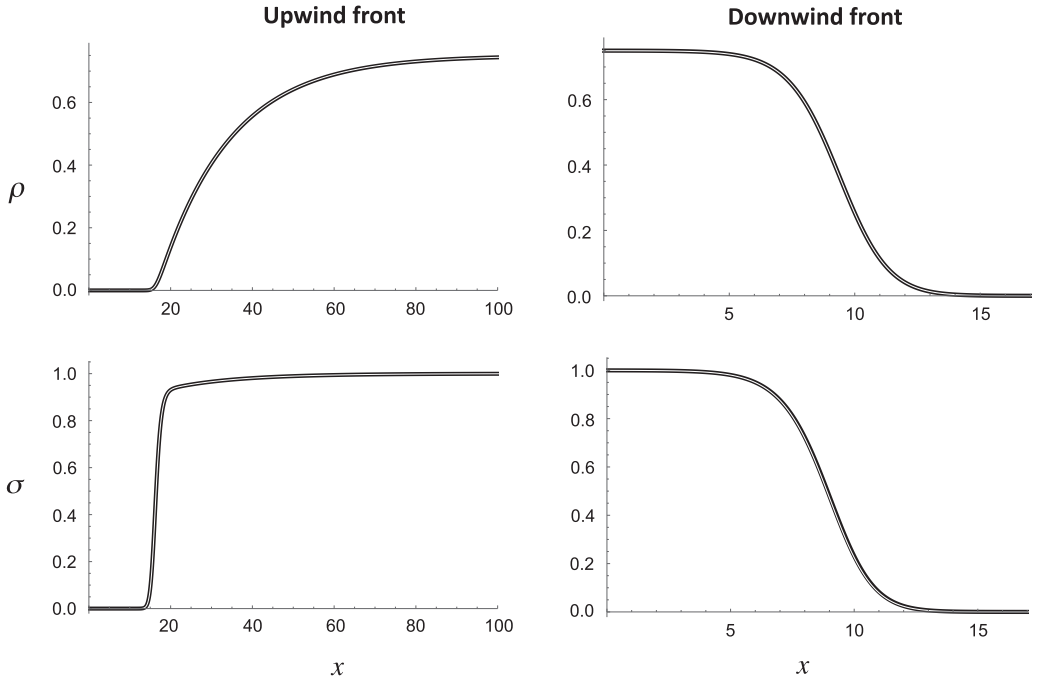

FIG. 13. Upwind (left column) and downwind (right column) fronts at $t = 176$ (thick, black), and at $t = 96$ (thin, white). Shown are profiles for both ρ (top row) and σ (bottom row). The parameters used were $a = 0.075$, $b = 0.1$, $d = 0.1$.

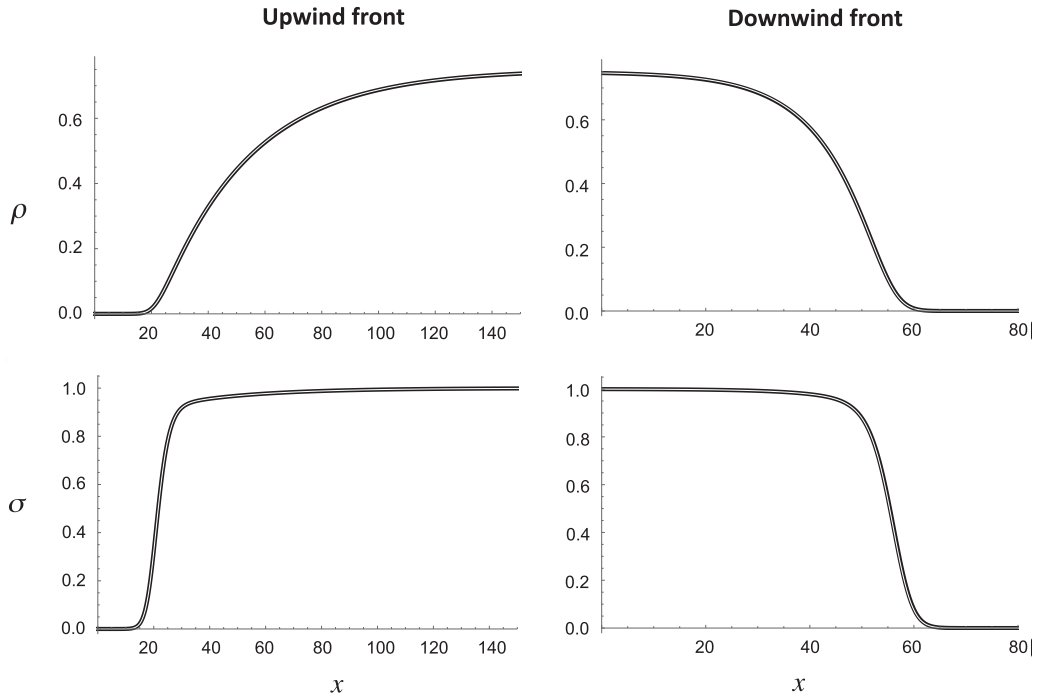

FIG. 14. Upwind (left column) and downwind (right column) fronts at $t = 176$ (thick, black), and at $t = 96$ (thin, white). Shown are profiles for both ρ (top row) and σ (bottom row). The parameters used were $a = 0.075$, $b = 0.1$, $d = 1$.

(exhibited at $a = 3$, $b = 1.5$, $\mathcal{D} = 0.1$, Fig. 15) and windward motion (exhibited at the other two parameters); an FKPP-like regime of $s_+^* \sim v_{\text{eff}} + 2\sqrt{\mathcal{D}_{\text{eff}}}$ behavior of the downwind front motion (exhibited at $a = 0.075$, $b = 0.1$, $\mathcal{D} = 1$, Fig. 14), and a non-FKPP-like regime (exhibited at the other two parameters).

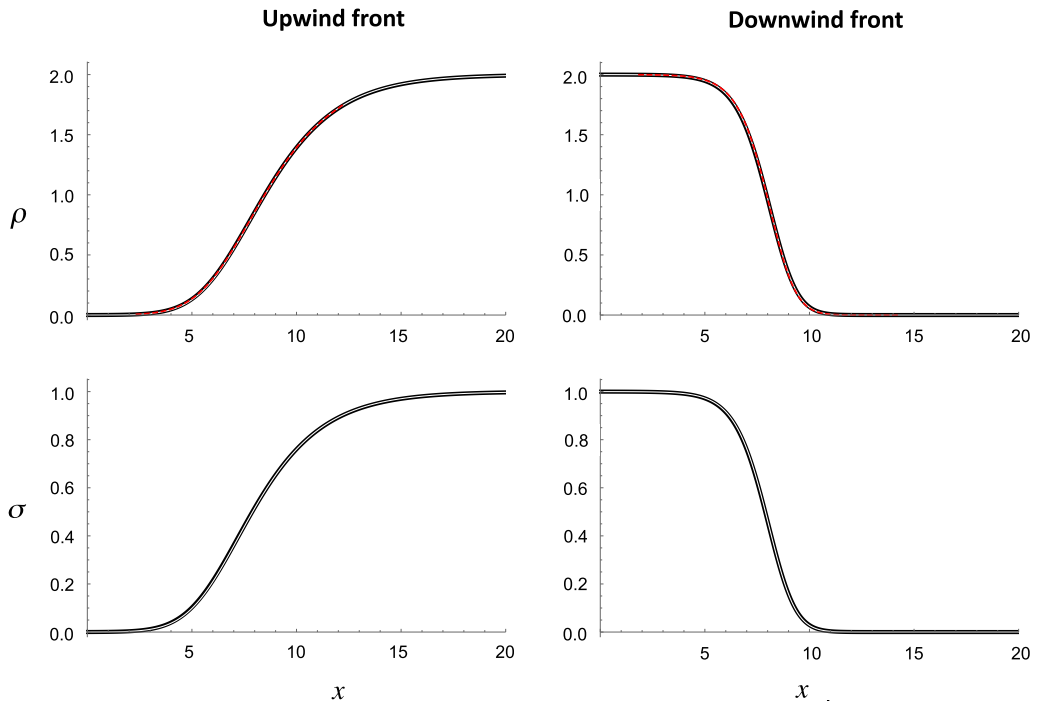

FIG. 15. Upwind (left column) and downwind (right column) fronts at $t = 176$ (thick, black), and at $t = 96$ (thin, white). Shown are profiles for both ρ (top row) and σ (bottom row). The parameters used were $a = 3.0$, $b = 1.5$, $d = 0.1$. Additionally, we show the heteroclinic solution of Eqs. (A1) and (A2) rescaled back to ρ and σ variables, that represents a UTF profile of ρ for both fronts (red, dashed curves). A shooting method was employed. We were not able to get a solution to come closer to the fixed point with $\rho = 2$, $\sigma = 1$, because of a strong divergence of trajectories due to the effect of a repelling manifold around that fixed point.

APPENDIX B: FULL SOLUTION OF THE LINEARIZED MODEL WITH ZERO DIFFUSION

In this section, we study the linearized problem. An exact solution to a δ-function IC will be given. The linearization of the nondimensionalized Eqs. (1) and (2) of the main text around the unstable state $\rho = \sigma = 0$, gives

$$\frac{\partial \rho}{\partial t} = -\frac{\partial \rho}{\partial x} + a\sigma - b\rho, \tag{B1}$$

$$\frac{\partial \sigma}{\partial t} = (1-a)\sigma + b\rho. \tag{B2}$$

We solve the problem by a Fourier Transform method. Let

$$\rho = A_\rho(k) e^{i\omega(k)t} e^{-ikx}, \tag{B3}$$

$$\sigma = A_\sigma(k) e^{i\omega(k)t} e^{-ikx}. \tag{B4}$$

The $\omega(k)$ and $\vec{A}(k)$ satisfy the following eigen-problem:

$$\omega \begin{pmatrix} A_\rho \\ A_\sigma \end{pmatrix} = \begin{pmatrix} k+ib & -ia \\ -ib & i(a-1) \end{pmatrix} \begin{pmatrix} A_\rho \\ A_\sigma \end{pmatrix}. \tag{B5}$$

The eigenvalues are given by

$$\omega = \frac{k - i(1-a-b)}{2} + \frac{1}{2}\sqrt{[k+i(1-a+b)]^2 - 4ab}. \tag{B6}$$

We now define the two branches. The square-root term can be expressed as

$$\tfrac{1}{2}\sqrt{(k-k_1)(k-k_2)},$$
$$\text{where} \quad k_1 = -i(1-a+b) - 2\sqrt{ab}, \quad k_2 = -i(1-a+b) + 2\sqrt{ab}, \tag{B7}$$

These $k = k_1$ and $k = k_2$ are branch points. We have the freedom in how we place the branch cut—a construction that ensures single-valuedness. Let $k - k_1 = \rho_1 e^{i\phi_1}$ and $k - k_2 = \rho_2 e^{i\phi_2}$, Fig. 17. We define each ϕ to be in $[-\pi, \pi]$. With this definition of angles, a path along a loop that encloses *both* branch points will not encounter multivaluedness, but a path around each single branch point will encounter a discontinuity of the exponential factor along a segment between k_1 and k_2. Therefore, with this definition of ϕs, the branch cut is a straight segment located between k_1 and k_2. Then

	"+" branch of the $\sqrt{}$	"−" branch of the $\sqrt{}$	$\Delta_- - \Delta_+$
Immediately above the cut	$\frac{i}{2}\sqrt{\rho_1\rho_2}$	$-\frac{i}{2}\sqrt{\rho_1\rho_2}$	$-i\sqrt{\rho_1\rho_2}$
Immediately below the cut	$-\frac{i}{2}\sqrt{\rho_1\rho_2}$	$\frac{i}{2}\sqrt{\rho_1\rho_2}$	$i\sqrt{\rho_1\rho_2}$

(B8)

Had we chosen a different definition of ϕs, the definition of a cut (and of branches) would also change. We will denote the two branches by $\pm$.

Unless $a = 1 + b$, a branch cut is not located on the real axis. When $a = 1 + b$, the portion of the real axis from $k = -\sqrt{ab}$ to $k = \sqrt{ab}$ still belongs to either one or the other branch. Thus, in plotting a dispersion relation versus the real k, no branch is crossed. A typical plot of a dispersion relation—$\omega_\pm$ versus (a real) k is shown in Fig. 16. The "+" branch of the $\mathrm{Im}[\omega(k)]$ curve is always positive. For $a < 1$, the "−" branch is entirely negative, and for $a > 1$, it is negative only over a range of $|k|$ below a certain value. Since the growth rate of a k mode is given by $e^{-\mathrm{Im}[\omega(k)]t}$, this indicates that all modes are unstable for $a < 1$, but large k modes become stable when $a > 1$. Physically, $a > 1$ means the rate of biotic mass production is less than the rate of leaving into the advective layer (AL). Thus, as a becomes larger and larger, biotic particles (such a spores) spend less and less time on the growth layer (GL). In the limit of infinite a they do not spend any time on the GL, and do not contribute to the growth, so $\sigma = \rho = 0$ becomes

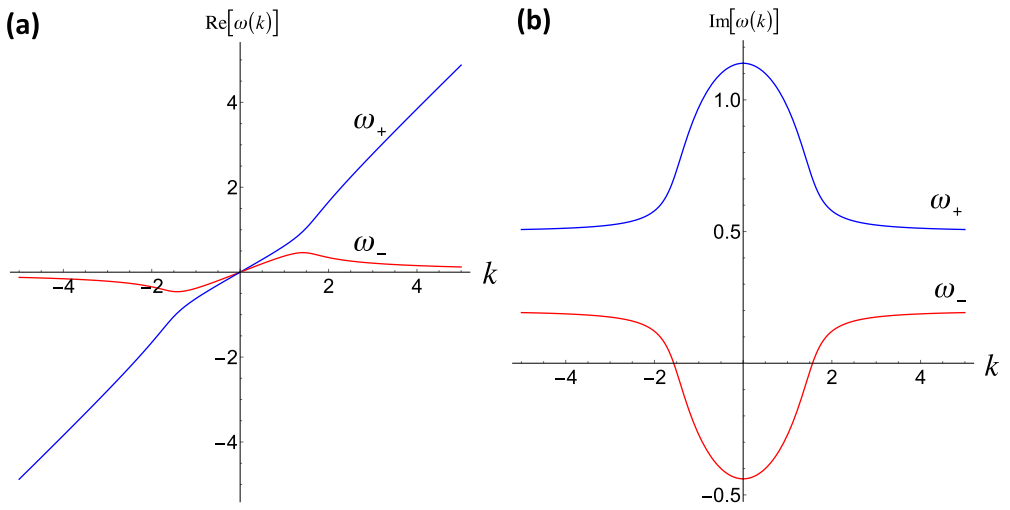

FIG. 16. (a) Re(ω) vs. k. (b) Im(ω) vs. k. Here the parameters were $a = 1.2$, $b = 0.5$.

a stable state. In fact, the whole "−" branch becomes marginally stable (zero). Similarly, if $a > 1$ and b goes to zero, the state $\sigma = \rho = 0$ also approaches marginality. The lowest value of the "−" branch is

$$-\mathrm{Im}[\omega_-(k=0)] = \frac{1-a-b}{2} + \frac{1}{2}\sqrt{(1-a+b)^2+4ab}. \tag{B9}$$

It is the inverse of the characteristic time scale for the growth of the most unstable ($k = 0$) mode. Notice that this equals $\lambda s_1(\lambda)$ at $\lambda = 0$, where s_1 is the + solution in Eq. (A4).

The corresponding eigenvectors are given by

$$\begin{pmatrix} A_\rho^\pm \\ A_\sigma^\pm \end{pmatrix} = \begin{pmatrix} \frac{C_\pm}{\sqrt{a^2-\Delta_\pm^2}} \\ \frac{iC_\pm\Delta_\pm}{\sqrt{a^2-\Delta_\pm^2}} \end{pmatrix}, \tag{B10}$$

$$\text{where} \quad \Delta_\pm \equiv \omega_\pm(k) - k - ib.$$

The $C_\pm$ are sign factors, and they will cancel out with sign factors in Fourier coefficients below. The general solution is an integral over all k of a linear combination of these two solutions:

$$\begin{pmatrix} \rho(x,t) \\ \sigma(x,t) \end{pmatrix} = \frac{1}{2\pi}\int_{-\infty}^{\infty} [\tilde\alpha(k)\vec A^+(k)e^{i\omega_+(k)t} + \tilde\beta(k)\vec A^-(k)e^{i\omega_-(k)t}]e^{-ikx}\,dk. \tag{B11}$$

The coefficients $\tilde\alpha(k)$ and $\tilde\beta(k)$ are determined from the ICs. Let the Fourier Transform of the IC be $\tilde\rho_0(k)$ and $\tilde\sigma_0(k)$. Then

$$\tilde\rho_0(k) = \tilde\alpha(k)A_\rho^+(k) + \tilde\beta(k)A_\rho^-(k),$$
$$\tilde\sigma_0(k) = \tilde\alpha(k)A_\sigma^+(k) + \tilde\beta(k)A_\sigma^-(k).$$

Solving for $\tilde\alpha(k)$ and $\tilde\beta(k)$, and substituting into Eq. (B11) we end up with

$$\rho(x,t) = \frac{1}{2\pi}\int_{-\infty}^{\infty} \frac{(\tilde\rho_0\Delta_- + ia\tilde\sigma_0)e^{i\omega_+t} - (\tilde\rho_0\Delta_+ + ia\tilde\sigma_0)e^{i\omega_-t}}{\Delta_- - \Delta_+} \times e^{-ikx}\,dk, \tag{B12}$$

and $\tilde\rho_0$, $\tilde\sigma_0$, $\Delta_\pm$, and $\omega_\pm$ are functions of k, as defined above. There is also (a more complicated) expression for $\sigma(x,t)$, but it is easier to extract σ using Eq. (B1) if we know ρ. The integral for ρ can be rewritten as

$$\rho(x,t) = \rho_{\mathrm{AL}}(x,t) + \rho_{\mathrm{GL}}(x,t), \tag{B13}$$

$$\rho_{\mathrm{AL}}(x,t) = \frac{1}{2\pi}\int_{-\infty}^{\infty} \tilde\rho_0(k)\left(\frac{\Delta_- e^{i\omega_+t} - \Delta_+ e^{i\omega_-t}}{\Delta_- - \Delta_+}\right)e^{-ikx}\,dk = \rho_{\mathrm{AL}}^+ - \rho_{\mathrm{AL}}^-, \tag{B14}$$

$$\rho_{\mathrm{GL}}(x,t) = \frac{ia}{2\pi}\int_{-\infty}^{\infty} \tilde\sigma_0(k)\left(\frac{e^{i\omega_+t} - e^{i\omega_-t}}{\Delta_- - \Delta_+}\right)e^{-ikx}\,dk = \rho_{\mathrm{GL}}^+ - \rho_{\mathrm{GL}}^-. \tag{B15}$$

Here ρ_{AL} is a contribution to $\rho(x,t)$ from the IC in the AL, and ρ_{GL} is a contribution to $\rho(x,t)$ from the IC on the GL. In this paper we will only be concerned with ICs on the GL. Therefore, to lighten the notation, the subscript "GL" in ρ_{GL} will be dropped, unless stated explicitly.

We will consider a special point-source initial distribution,

$$\sigma_0(x) = M\delta(x), \tag{B16}$$

that has a fourier transform given by M in all of k space. An exact solution will be given for this type of IC. We will also consider an exponentially localized ICs

$$\sigma_0(x) = \frac{M\mu}{2}e^{-\mu|x-x_0|}. \tag{B17}$$

x_0 can be set to 0 without loss of generality, since in this problem the coefficients a and b are homogeneous. The fourier transform of such an IC is

$$\tilde\sigma_0(k) = \frac{M}{1+(k/\mu)^2}. \tag{B18}$$

The solution with this IC in the limit $\mu \to \infty$ should be identical to the solution with δ-function IC. The behavior of other IC that have a finite, but nonpoint support should approach the behavior of solutions with a δ-function IC at distances much greater than the extent of this support. Since the main interest of this paper concerns with long-range transport, we will not make explicit calculations for other compact IC. We remark that ICs with power-law tails give rise to accelerating wave fronts, while Gaussian ICs behave as a point sources.

The integrals in Eqs. (B14) and (B15) are taken along the real line in k space, but close the contour (which is possible, since the branch cuts are finite segments with our definition of branches of the square root) we have to discuss the behavior of $\omega_\pm$ as $|k| \to \infty$. There are two branches of ω and they differ by a sign. Thus, as $|k|$ gets large, $\omega_\pm \sim \frac{k}{2} \pm \frac{k}{2} + O(\frac{1}{k})$. So $\omega_+ \sim k$, and

$$e^{i\omega_+t}e^{-ikt} \sim e^{ik(t-x)}$$

at large $|k|$. Evidently, the contour of the ρ^+-integral will have to be closed in the lower half-plane for $x > t$ and in the upper half-plane for $x < t$. The ω_- branch does not have an important k-dependence at large $|k|$, so

$$e^{i\omega_-t}e^{-ikx} \sim e^{-ikx}$$

at large $|k|$. The contour of the ρ^--integral will have to be closed in the lower half-plane for $x > 0$ and in the upper half-plane for $x < 0$. Table I summarizes the contours.

The two types of features of the integrand that these contours may enclose are: *poles* at $k = \pm i\lambda$ that are present only for exponential ICs, but not compact ICs, and a *branch cut segment* that is present for any IC, Fig. 17. Its center is located at position $-i(1-a+b)$, so it will be located in the upper half-plane for $a > 1+b$ and in the lower half-plane for $a < 1+b$. A semicircular contour may be shrunk to enclose only these features. Thus, if a contour encloses a pole and a

TABLE I. Summary of integration contours

	$x < 0$	$0 < x < t$	$x > t$
ρ^+ integral	Above	Above	Below
ρ^- integral	Above	Below	Below

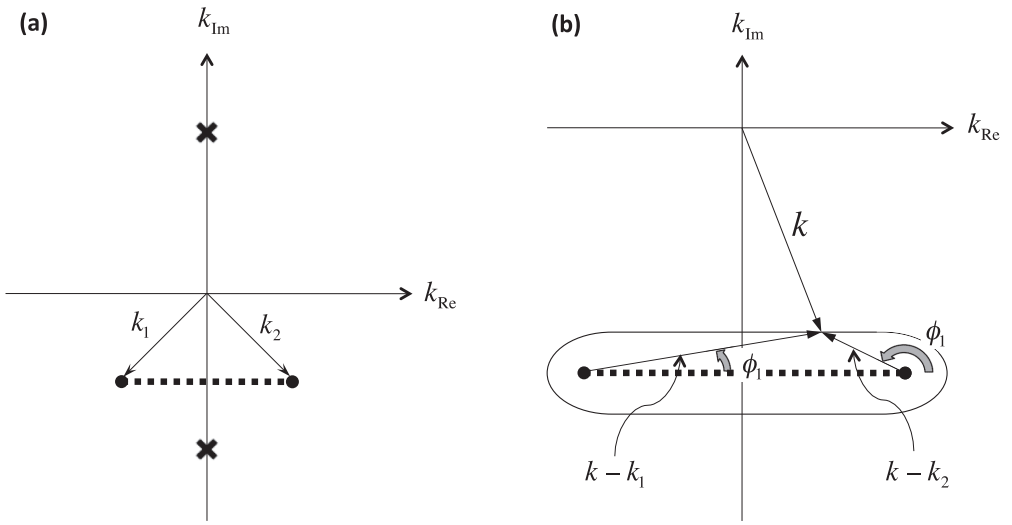

FIG. 17. (a) Features in the k space: dashed, branch cut; crosses, poles. (b) Cartoon of a contour around the branch cut. The contour lies infinitesimally close to the cut.

branch cut, there will be a pole contribution and a branch cut contribution.

With these considerations in mind, the total integral (this is in fact true for either ρ_{GL} or ρ_{AL}) is summarized in Table II below. Here, the pole$_+$ and pole$_-$ refers to the position of the pole—the one in the upper half-plane or in the lower half-plane, respectively; same for a branch cut. It will turn out that the branch cut contributions for either $x<0$ or $x>t$ will cancel and only poles contribute to the solution in these regions. Thus, if we start with a localized IC (when there are no poles), ρ (and σ) will be zero in these regions, as expected, since the wind cannot carry material backwards, and material also cannot arrive to a point x faster than the wind (which has speed 1 in these units). Note: when $a=1+b$, the branch cut segment lies right on the real axis. However, we may move the original contour off the real axis by an infinitesimal amount, close the contour as specified above, and shrink it to enclose the branch cut segment and the pole. Alternatively, we may treat the case $a=1+b$ as a limit, because it is unique—as we will see, the resulting limit for ρ and σ is the same, whether the limit approaches $1+b$ from above or from below.

The contour around the cut consists of a straight line segment right above the cut, the straight line segment right below the cut, and two infinitesimal semicircles around each end of the cut. It is easy to show that their contributions goes to zero in the limit as the radius of these semicircles go to zero. The directions of integration above and below the cut are opposing each other, but these pieces do not cancel because because the value of both branches of ω differs right above and right below the cut, as specified in Eq. (B8). Then

$$\rho^+\text{-BC}_- = \frac{ia}{2\pi}\int_{k_1}^{k_2}\frac{M}{1+(k/\mu)^2}\frac{e^{-ikx}e^{i\frac{[k-i(1-a-b)]t}{2}}e^{-\frac{t}{2}\sqrt{\rho_1\rho_2}}}{-i\sqrt{\rho_1\rho_2}}\,dk + \frac{ia}{2\pi}\int_{k_1}^{k_2}\frac{M}{1+(k/\mu)^2}\frac{e^{-ikx}e^{i\frac{[k-i(1-a-b)]t}{2}}e^{\frac{t}{2}\sqrt{\rho_1\rho_2}}}{-i\sqrt{\rho_1\rho_2}}\,dk, \tag{B19}$$

$$\rho^-\text{-BC}_- = \frac{ia}{2\pi}\int_{k_1}^{k_2}\frac{M}{1+(k/\mu)^2}\frac{e^{-ikx}e^{i\frac{[k-i(1-a-b)]t}{2}}e^{\frac{t}{2}\sqrt{\rho_1\rho_2}}}{-i\sqrt{\rho_1\rho_2}}\,dk + \frac{ia}{2\pi}\int_{k_1}^{k_2}\frac{M}{1+(k/\mu)^2}\frac{e^{-ikx}e^{i\frac{[k-i(1-a-b)]t}{2}}e^{-\frac{t}{2}\sqrt{\rho_1\rho_2}}}{-i\sqrt{\rho_1\rho_2}}\,dk. \tag{B20}$$

If the branch cut is above the real axis, the integrals gain a minus sign, since the contour is oriented in the opposite direction, i.e., $\rho^+\text{-BC}_+ = -\rho^+\text{-BC}_-$ and $\rho^-\text{-BC}_+ = -\rho^-\text{-BC}_-$. We see immediately that $\rho^+\text{-BC}_\pm = \rho^-\text{-BC}_\pm$. All these considerations allow us to simplify Table II, which now takes the form of Table III.

Only poles contribute outside of $0<x<t$, as expected. Letting $k=k_c+l\xi$, where $k_c=-i(1-a+b)$ and

TABLE II. Total ρ for different regions of space.

	$x<0$	$0<x<t$	$x>t$
$a<1+b$	$\rho^+\text{-pole}_+ - \rho^-\text{-pole}_+$	$\rho^+\text{-pole}_+ - (\rho^-\text{-pole}_- + \rho^-\text{-BC}_-)$	$(\rho^+\text{-BC}_- + \rho^+\text{-pole}_-)$ $-(\rho^-\text{-BC}_- + \rho^-\text{-pole}_-)$
$a>1+b$	$(\rho^+\text{-BC}_+ + \rho^+\text{-pole}_+)$ $-(\rho^-\text{-BC}_+ + \rho^-\text{-pole}_+)$	$(\rho^+\text{-BC}_+ + \rho^+\text{-pole}_+) - \rho^-\text{-pole}_-$	$\rho^+\text{-pole}_- - \rho^-\text{-pole}_-$

TABLE III. Total ρ for different regions of space.

	Region I: $x < 0$	Region II: $0 < x < t$	Region III: $x > t$
Any a or *b*	ρ^+-pole$_+$ − ρ^--pole$_+$	(ρ^+-pole$_+$ − ρ^--pole$_-$) − ρ^--BC$_-$	ρ^+-pole$_-$ − ρ^--pole$_-$

$l = 2\sqrt{ab}$—half of the width of the branch cut—we have

$$-\rho^-\text{-BC}_- = \frac{aMe^{-\kappa(x-wt)}}{2\pi}\left[\int_{-1}^{1}\frac{e^{-iA\xi}e^{-B\sqrt{1-\xi^2}}}{\sqrt{1-\xi^2}}\frac{d\xi}{1+\left(\frac{k_c+l\xi}{\mu}\right)^2} + \int_{-1}^{1}\frac{e^{-iA\xi}e^{B\sqrt{1-\xi^2}}}{\sqrt{1-\xi^2}}\frac{d\xi}{1+\left(\frac{k_c+l\xi}{\mu}\right)^2}\right], \tag{B21}$$

$$\kappa = 1-a+b,$$
$$w = \frac{1-a}{1-a+b},$$
$$A = 2\sqrt{ab}\left(x-\frac{t}{2}\right),$$
$$B = t\sqrt{ab}. \tag{B22}$$

We now confront the integrals in Eq. (B21). The parameter B becomes greater than 1 for $t > 1/\sqrt{ab}$, after which time the second integral becomes rapidly dominant. Now, let $\xi = \sin y$. Then, the remaining integral is

$$\mathcal{I} = \int_{-\pi/2}^{\pi/2}\frac{e^{-iA\sin y}e^{B\cos y}}{1+\left(\frac{k_c+l\sin y}{\mu}\right)^2}dy. \tag{B23}$$

We may extend the limits of integration to $[-\pi,\pi]$ with very little error, because $\cos y$ is negative in this extra region, and the exponent contains a large positive B. Then, using the trigonometric identity, we have

$$\mathcal{I} \approx \int_{-\pi}^{\pi}\frac{e^{\sqrt{B^2-A^2}\cos(y-y_0)}}{1+\left(\frac{k_c+l\sin y}{\mu}\right)^2}dy, \tag{B24}$$

where $\sin y_0 = \frac{-iA}{\sqrt{B^2-A^2}}$ and $\cos y_0 = \frac{B}{\sqrt{B^2-A^2}}$. The factor in the exponent is

$$\sqrt{B^2-A^2} = 2\sqrt{ab}\sqrt{x(t-x)}. \tag{B25}$$

Point IC in the GL

For a δ-function IC, there are no pole contributions. Furthermore, the denominator in the integrand in Eqs. (B23) or (B24) will be simply 1. In this special case the answer turns out to be

$$\mathcal{I} = 2\pi I_0[2\sqrt{ab}\sqrt{x(t-x)}], \tag{B26}$$

where I_0 is the modified Bessel function of the first kind. And thus,

$$\rho(x,t) = -\rho^-\text{-BC}_- \approx aMe^{-\kappa(x-wt)}I_0[2\sqrt{ab}\sqrt{x(t-x)}] \tag{B27}$$

[see Eq. (B21)]. Although this is technically an approximation, it works very well for all but the very early times ($\ll 1/\sqrt{ab}$).

We can substitute this result into Eqs. (B1) and (B2) and obtain

$$\sigma(x,t) \approx \sqrt{ab}Me^{-\kappa(x-wt)}I_1(2\sqrt{ab}\sqrt{x(t-x)})\frac{t-x}{\sqrt{x(t-x)}}. \tag{B28}$$

1. Propagation speed and decay rates of tails

We can extract the speed of the propagation as well as the decay rate of solution tails. First, we use the asymptotic approximation for both $I_0(z)$ and $I_1(z) \sim \frac{e^z}{\sqrt{2\pi z}}$, so both $\rho(x,t)$ and $\sigma(x,t)$ have the following exponential behavior in x and t:

$$\rho(x,t),\sigma(x,t) \sim e^{-\kappa(x-wt)+2\sqrt{ab}\sqrt{x(t-x)}}. \tag{B29}$$

We will now solve for $x_c(t)$—the movement of the intersection of $\rho(x,t)$ with a contour of constant value c. First ignoring the nonexponential factors, we have

$$\frac{2abt+\kappa(c+\kappa tw)\pm 2\sqrt{ab\{abt^2-[c+\kappa t(w-1)](c+\kappa tw)\}}}{4ab+\kappa^2}.$$

In the long time limit, we get

$$x_c(t) = \frac{t}{1+\frac{b}{(1\pm\sqrt{a})^2}}. \tag{B30}$$

The value of c enters into the corrections that grow slower than c; it affects the time required to develop this asymptotic behavior linear in time. Had we included the nonexponential prefactor, there would be a logarithmic in time correction to $x_c(t)$. Thus, the speed will still relax to the above value.

We can now switch to the comoving variables $x = \frac{t}{1+\frac{b}{(1\pm\sqrt{a})^2}} + z$. Ignoring the nonexponential prefactor, the result is

$$\rho(z,t),\sigma(z,t) \sim e^{-\lambda_\pm^* z \mp \frac{\sqrt{a}(\lambda_\pm)^3}{4bt}z^2+\cdots}, \tag{B31}$$

with $\lambda_\pm^*$ being given by Eq. (5) from the main text. Thus, in the long-time limit, the leading-order term is $e^{-\lambda_\pm^* z}$—a function of $x - s_\pm^* t$. We also see the power-law relaxation to both speed and the stationary tail shape, in agreement with the general theory of fronts [19]. Thus, we reproduced the formula for the front speed $s_\pm^*$ [Eq. (4) in the main text] and the exponential contribution to the shape of the density tails [Eq. (5) in the main text]—both of which we obtained by other methods (see the previous and the following sections).

2. Zero growth case

We now address an important special case of zero growth, which describes the movement of nonreproducing passive scalar, such as dust. In terms of physical parameters, this is

described by

$$\frac{\partial \rho}{\partial t} = -v_0 \frac{\partial \rho}{\partial x} + \alpha\sigma - \beta\rho, \tag{B32}$$

$$\frac{\partial \sigma}{\partial t} = (1-\alpha)\sigma + \beta\rho. \tag{B33}$$

We can retrace the entire derivation involving the contour integration, which now represents the exact solution. For example,

$$\rho \approx \frac{M\alpha}{v_0} e^{(\frac{\alpha-\beta}{v_0})(x-\frac{\alpha v_0}{\alpha-\beta}t)} I_0\left[\frac{2\sqrt{\alpha\beta}}{v_0}\sqrt{x(v_0 t - x)}\right]. \tag{B34}$$

We will find the identical result if we switch Eq. (B27) to physical variables (note: in the full model with nonlinearity, we rescaled densities by $\sigma_{\max}$, which also makes them dimensionless. In the linearized model for which Eq. (B27) is a solution, there is no $\sigma_{\max}$, so densities should be non-dimensionalized by multiplying by δ/v_0 instead, since this is the natural measure of 1/distance. Taking this into account is necessary to recover the result in Eq. (B34)). This solution describes a pulse, the width of which grows as $\sqrt{t}$—so it has no defined stationary limit. Note that if we take Eq. (5) and switch to physical units, we get a profile width that grows as $1/\sqrt{\delta}$ when $\delta \to 0$. This reflects the fact that at $\delta = 0$, ρ and σ become a permanently transient solution—the tails do not reach a stationary shape. The speed of the profile peak is $\frac{v_0}{1+\beta/\alpha}$—exactly the prediction of the general formula for either front if $\delta \to 0$. The magnitude of the peak decays as $1/t$. In the vicinity of the peak, the solution is

$$\rho \approx \frac{\alpha M}{2v_0\sqrt{\pi}t}\sqrt{\frac{\alpha+\beta}{\alpha\beta}}\exp\left(-\frac{(\alpha+\beta)^3\xi^2}{4\alpha\beta v_0^2 t}\right), \tag{B35}$$

where $\xi = x - x_{\text{peak}}$. The total mass under this profile is conserved—it is given by $\frac{M}{1+\beta\alpha}$. Similarly to the speed, this is simply related to the fraction of the time spent in the advective layer. We can also obtain this number by integrating Eqs. (B32) and (B33) over all space and imposing the constraint that the sum of the mass in both layers is a constant.

APPENDIX C: ALTERNATIVE DERIVATION OF SPEEDS AND DECAY LENGTHS USING THE SADDLE-POINT METHOD

We here show how to find the speed of pulled density fronts using a saddle-point approximation, as an alternate technique. The motivation for doing this is to corroborate the results derived in the main paper. This technique was taken from a comprehensive review on front propagation by W. von Saarloos [19]. We first recite the derivation of the technique and then apply it to our problem.

1. Method summary

Consider a solution of the full, nonlinear equation propagating into the zero-density linearly unstable state. The smallness of the density in the leading part of the propagating profile suggests that dynamics of those regions, along with their properties (speed, decay rate, etc.) may be extracted from the linearized equations of motion. This is not always true, because these leading tails are matched to the part of the density profile where the nonlinearities do become important. However, in many cases this idea is correct. A front of the nonlinear partial differential equation (PDE) is said to be *pulled*, if its speed—defined by the speed measured at a constant density—is identical to the speed under the linearized dynamics.

In light of this, we consider a scalar field $\phi(x,t)$, whose dynamics is determined by a translationally invariant linear PDE, obtained by linearizing the full equation of motion around the state $\phi = 0$, and express this solution as a Fourier Transform:

$$\phi(x,t) = \frac{1}{2\pi}\int_{-\infty}^{\infty} dk \bar{\phi}_0(k) e^{-i[kx-\omega(k)t]}. \tag{C1}$$

Here, $\omega(k)$ is the dispersion relation, which can be found, for instance, by substituting the Fourier ansatz $e^{i(kx-\omega t)}$ into the governing linear equations. We assume $\phi = 0$ is a linearly unstable solution; i.e., the amplitude of some of the Fourier modes grow in time under the linearized equations. From Eq. (C1), these are the modes with wave number k for which Im $\omega(k) > 0$. Because these modes are unstable, a typical localized IC will give rise to a disturbance that grows and spreads out in time under the linearized dynamics. We define the speed of the profile to be the asymptotic speed of the point of constant contour:

$$s_0 = \lim_{t\to\infty} \frac{dx_{c_0}}{dt}, \tag{C2}$$

where $\phi(x_{c_0},t) = c_0$. The resulting speed is independent of the value of c_0 due to linearity of the governing PDE. In general, disturbances could propagate to the left and to the right. The method outlined here is general, and we would need to distinguish between multiple solutions for the speed.

The speed s_0 can be determined self-consistently by making the following key observation: it is the speed of such a reference frame, from which the density profile looks stationary after the transients decay. Let z denote the coordinate in the co-moving frame: $z = x - s_0 t$. Then

$$\begin{aligned}\phi(z,t) &= \frac{1}{2\pi}\int_{-\infty}^{\infty} dk \bar{\phi}_0(k) e^{-i\{(kx-ks_0t)-[\omega(k)t-s_0kt]\}} \\ &= \frac{1}{2\pi}\int_{-\infty}^{\infty} dk \bar{\phi}_0(k) e^{-ikz+it[\omega(k)-s_0k]}.\end{aligned} \tag{C3}$$

If $\bar{\phi}_0$ is analytic everywhere in the complex plane, we can compute this integral when t is large using a saddle-point approximation—finding the k^* at which the term $\omega(k) - s_0 k$ has a saddle point, and expanding that term to quadratic order [the function $\omega(k)$ is also assumed to be analytic in the vicinity of its extrema, so this extrema can only be saddles]. This k^* is given by

$$\frac{d}{dk}[\omega(k) - s_0 k]_{k^*} = 0. \tag{C4}$$

This leads to our first expression for the speed s_0,

$$s_0 = \left.\frac{d\omega}{dk}\right|_{k^*}. \tag{C5}$$

The integrand in Eq. (C3) will be proportional to: $e^{-ik^*z}e^{it[\omega(k^*)-s_0k^*]}$. From our earlier observation, we require

that $\phi(z)$ neither grows nor decays. This means that

$$\mathrm{Im}[\omega(k^*) - s_0 k^*] = 0, \tag{C6}$$

which leads to our second expression for s_0,

$$s_0 = \omega_i^*/k_i^*. \tag{C7}$$

Here, the r and i subscripts denote real and imaginary part of complex quantities. We can find k^* by equating Eqs. (C6) and (C7) and then substitute this back into Eq. (C7) to obtain our desired expression for s:

$$\left.\frac{d\omega}{dk}\right|_{k^*} = \omega_i^*/k_i^* \qquad \Rightarrow \text{Find } k^*, \tag{C8}$$

$$s = \omega_i^*/k_i^* \qquad \Rightarrow \text{Find } s. \tag{C9}$$

We can also compute an approximation to the wave profile ϕ. Expanding the term $\omega(k) - s_0 k$ in Eq. (C3) to second order around k^* and taking into account Eqs. (C4) and (C6), results in the following saddle-point approximation:

$$\begin{aligned}\phi(z,t) &\approx \frac{1}{2\pi}\bar{\phi}_0(k^*)e^{-ik^*z}\int_{-\infty}^{\infty} dk e^{[it(\omega_r^* - s_0 k_r^*) - Dt(\Delta k)^2]} \\ &= \frac{1}{\sqrt{4\pi Dt}}\bar{\phi}_0(k^*)e^{-i(k_r^* z - \omega_r^* t + s_0 k_r^* t)}e^{k_i^* z}e^{\frac{-z^2}{4Dt}},\end{aligned} \tag{C10}$$

where $\Delta k = k - k^*$ and $D = -(i/2)\omega''(k^*)$. We must also prohibit oscillatory solutions, since the density cannot be negative. Therefore, we require that $(k_r, \omega_r, D_i) = (0,0,0)$. This result will help us to eliminate certain solutions when s_0 is multivalued. The resulting nonoscillatory expression can be written as

$$\phi(z,t) \approx \frac{1}{\sqrt{4\pi D}}\bar{\phi}_0(k^*)e^{k_i^* z - \frac{1}{2}\ln t - \frac{z^2}{4Dt}}. \tag{C11}$$

Aside from the logarithmic error, which is a consequence of a Gaussian approximation of the integrand, this function becomes time-independent at large times, as planned. One must also check that $D_r > 0$, for physically meaningful solutions. The sign of k_i^* helps us to distinguish between the downwind and upwind flanks of the solution of the linear equation (these are respectively the analogues of the downwind and upwind fronts, which are properties of solutions of the parent nonlinear equation). For the downwind flank, we require $k_i^* < 0$, so the profile is exponentially decaying for increasing x. For the upwind flank, we require $k_i^* > 0$, so the profile is exponentially increasing for increasing x.

Eqs. (C8), (C9), and (C10) summarize our results. They allow us to determine the properties of the tail of a pulled front, including its front speed s, and the growth or decay rate k_i^*. The only requirement for their use is the dispersion relation $\omega(k)$ and analyticity of $\bar{\phi}_0(k)$.

In summary:

(1) Find dispersion relation $\omega(k)$: Substitute $\phi(x,t) = e^{-i(kx-\omega(k)t)}$ into linearized PDE.

(2) Find k^*: $\frac{d\omega}{dk}|_{k^*} = \omega_i^*/k_i^*$.

(3) Find speed $s_0 = \omega_i^*/k_i^*$, and decay (for the downwind flank) or growth (for the upwind flank) rate k_i^*.

(4) Enforce $(\omega_r^*, k_r^*, D_i) = (0,0,0)$ for nonoscillating solution.

Multiple solutions for k^* are possible, stemming from the fact that the method is not restricted to a specific IC, as long as the Fourier Transform of the IC is an entire function in k space.

2. Application to our problem

We now apply these results to our problem. The front speed will depend on the three parameters: $s_0(a,b,\mathcal{D})$. We first solve the $\mathcal{D} = 0$ case and then consider the more realistic situation when $\mathcal{D} \neq 0$. The * will be dropped.

a. Without diffusion

The dispersion relation $\omega(k)$ has already been found for this case—see Eqs. (B3)–(B6). It satisfies

$$\omega^2 - i\omega(a + b - ik - 1) + b - ik(1 - a) = 0. \tag{C12}$$

We can follow the procedure advertised above: find (k_r, k_i) of the saddle point and compute ω at this k. However, ω is a multivalued function, and this would require keeping track of the branches. On the other hand, note that Eqs. (C12) and (C8) constitute a set of four algebraic equations in the variables $(\omega_i, \omega_r, k_r, k_i)$. From Eq. (C9), we can substitute $\omega_i = s_0 k_i$, to obtain a set of equations in the variables $(s_0, \omega_r, k_r, k_i)$. There are six solutions, two of which have $(k_r = 0 = \omega_r)$. These are

Solution	s_0	k_i	D_r
1	$\frac{1}{1+\frac{b}{(1-\sqrt{a})^2}}$	$-\frac{1+a+b-2\sqrt{a}}{1-\sqrt{a}}$	$\frac{(\sqrt{a}-1)^3 b}{\sqrt{a}(1+a+b-2\sqrt{a})^3}$
2	$\frac{1}{1+\frac{b}{(1+\sqrt{a})^2}}$	$-\frac{1+a+b+2\sqrt{a}}{1+\sqrt{a}}$	$\frac{(\sqrt{a}+1)^3 b}{\sqrt{a}(1+a+b+2\sqrt{a})^3}$

(C13)

We identify the two speeds as those of the upwind and downwind fronts, $s_\pm$, cf. Eq. (4) in the main text. The leading term in the spatial profile is given by $\phi \sim e^{k_i z} \equiv e^{-\lambda z}$. The corresponding λ also match with Eq. (5) of the main text. The D_r also matches the predictions of Eq. (B31).

To be consistent, we require that $k_i^{(2)} < 0$ for $s_0^{(2)}$ to correspond to the speed of the downwind flank. Inspecting the table above, we see that this is indeed the case. We similarly require that $k_i^{(1)} > 0$ for $s_0^{(1)}$ to be the speed of the upwind flank. Here the situation is not as clear cut. One can show that $k_i^{(1)} > 0$ only when $a > 1$. This is consistent with our observation in the main text that the upwind flank moves only when $a > 1$. But for $a < 1$, $k_i^{(2)} < 0$, indicating that $s_0^{(2)}$ is *another* possible wave speed for the downwind flank. Here the sign of D helps to select the branch: $D^{(1)}$ is negative for $a < 1$, so this is an unphysical solution, and we must select $s^{(2)}$ as the speed of the downwind flank for any a.

b. With diffusion

We repeat the same procedure as before. With the inclusion of diffusion, the dispersion relation is now satisfied by

$$\begin{aligned}&\omega^2 - i\omega(a + b + \mathcal{D}k^2 - ik - 1) \\ &\quad - ik(1 - a - \mathcal{D}k^2) - b\mathcal{D}k^2 + b = 0.\end{aligned} \tag{C14}$$

As before, this determines a set of four algebraic equations in the variables $(s_0, \omega_r, k_r, k_i)$. By imposing $(\omega_r, k_r) = (0, 0)$,

we get four solutions for the speed ($s^{(1)}$, $s^{(2)}$, $s^{(3)}$, $s^{(4)}$), which are all functions of the parameters (a, b, $\mathcal{D}$). The expressions are complicated, involving roots of sixth-degree polynomials.

The first of these solutions has $k_i^{(1)} > 0$, for all parameter ranges, indicating $s^{(1)}$ corresponds to the speed of the upwind flank. From plotting this solution, we find it corresponds exactly to the solution plotted in Fig. 4(b) of the main text. The remaining three solutions never have $k_i > 0$, so they refer to the downwind flank. Unlike in the $\mathcal{D} = 0$ case, the constraint that D is positive and real does not narrow down the candidates to a single solution. We point out, however, that the values of $-k_i$ match the values of λ at which the extrema of the $s(\lambda)$ take place for $\lambda > 0$ (see Figs. 6 and 7). According to Ref. [19]—for pulled fronts, ICs with a compact support will select the λ at which the branch of $s(\lambda)$ with the largest speed has a minimum.

APPENDIX D: PROPERTIES OF STATIONARY BACKGROUNDS IN THE $\mathcal{D} = 0$ MODEL FOR $a \leqslant 1$

We briefly discuss the stationary wake, such as section I in Fig. 2(a), and conditions for its existence. Setting to zero the time derivatives in (nondimensionalized) Eqs. (1) and (2) with zero diffusion, gives the following equation for $\sigma_{\rm st}(x)$:

$$\frac{d\sigma_{\rm st}}{dx} = bf(\sigma_{\rm st})\left(a - \frac{df}{d\sigma_{\rm st}}\right)^{-1}, \tag{D1}$$

while $\rho_{\rm st}(x)$ follows from from Eq. (2). When an IC is 0 for $x < 0$, the boundary condition for this equation, $\sigma(x = 0)$, is given by a σ_0 that satisfies $f(\sigma_0) = a\sigma_0$. This follows from $\rho_{x=0} \to 0$ for large times and from Eq. (2).

If $\sigma_0 > 0$, there exists a stationary solution that approaches 1 over a characteristic length given by $(d - a)/bd$, where $d = \frac{df}{d\sigma}|_{\sigma=1}$ ($d = -1$ for logistic case). This is true for all concave $f(\sigma)$. On the other hand, if $\sigma_0 = 0$ there is no nonzero stationary state for $\sigma(x)$ and $\rho(x)$, since $f(0) = 0$. This happens for all concave $f(\sigma)$ when $a > 1$ or, more generally, when the transfer rate from σ to ρ exceeds the growth rate $[a\sigma > f(\sigma)]$ at any $0 < \sigma < 1$ (and the IC has a finite support). The mass is swept by the AL downwind; $\sigma(x,t)$ and $\rho(x,t)$ become pulse waves. The two fronts of the pulse propagate with different speeds, as discussed in the main text.

APPENDIX E: NUMERICAL METHOD

1. Preliminary calculations

Before discussing the method, it will be useful to prove that the model without diffusion does not admit shocks. This is important, because it makes use of special numerical methods, that otherwise must be employed to keep track of the movement of shock waves, unnecessary. The dimensionless version of Eqs. (1) and (2) from the main text can be converted to a single second-order equation for either σ or ρ. For example,

$$\frac{\partial^2\sigma}{\partial t^2} + \frac{\partial^2\sigma}{\partial t\partial x} + \frac{\partial\sigma}{\partial t}(a + b - 1 + 2\sigma) + \frac{\partial\sigma}{\partial x}(a - 1 + 2\sigma) = 2f(\sigma). \tag{E1}$$

A similar equation can be derived for ρ. In both cases, they have the form

$$\frac{\partial^2\phi}{\partial t^2} + \frac{\partial^2\phi}{\partial x\partial t} = F\left(\phi, \frac{\partial\phi}{\partial t}, \frac{\partial\phi}{\partial x}\right). \tag{E2}$$

From this, it can be easily shown [28] that characteristics $x(t)$ obey

$$\left(\frac{dx}{dt}\right)^2 - \left(\frac{dx}{dt}\right) = 0. \tag{E3}$$

The two pairs of families of characteristics are thus $x = c_1$ and $x = t + c_2$, where c_1 and c_2 are arbitrary real constants. Evidently, characteristics in each family do not intersect each other, proving the absence of shocks.

2. Outline of the numerical methods and parameters used

We used the first-order time-differencing scheme,

$$\left.\frac{\partial\phi}{\partial t}\right|_{x_m,t_n} \to \frac{\phi(x_m,t_{n+1}) - \phi(x_m,t_n)}{\Delta t}, \tag{E4}$$

and an upwind spatial differencing scheme,

$$\left.\frac{\partial\phi}{\partial x}\right|_{x_m,t_n} \to \frac{\phi(x_m,t_n) - \phi(x_{m-1},t_n)}{\Delta x}. \tag{E5}$$

With this discretization, our equations become

$$\rho(x_m,t_{n+1}) = \rho(x_m,t_n)(1 - b\Delta t - \Delta t/\Delta x) + \sigma(x_m,t_n)a\Delta t + \rho(x_{m-1},t_n)\Delta t/\Delta x, \tag{E6}$$

$$\sigma(x_m,t_{n+1}) = \sigma(x_m,t_n)(1 - a\Delta t) + f(\sigma(x_m,t_n))\Delta t + \rho(x_m,t_n)b\Delta t + \frac{\mathcal{D}\Delta t}{(\Delta x)^2}[\sigma(x_{m+1},t_n) - 2\sigma(x_m,t_n) + \sigma(x_{m-1},t_n)], \tag{E7}$$

where $x_m = x_0 + m\Delta x$ and $t_n = t_0 + n\Delta t$. Thus, this is an explicit method; i.e., it uses known data at time step t_n to march a solution forward in time to t_{n+1}.

The integration took place over a finite spatial interval, with an initial condition placed in the center. At the extreme left and extreme right points of this spatial interval, we set the values of ρ and σ to zero (these points were not included in any plots or analyses). For $\mathcal{D} = 0$ case, the value of ρ and σ at the right boundary is irrelevant, since information does not propagate backwards with our scheme. The existence of the boundary condition on the left is irrelevant as long as IC has a finite support (and zero to the left of the this support region), and the left edge of this support is at least one grid point away from the left edge of the spatial interval. Conversely, the boundary condition used on the left is equivalent to setting the left edge to a localized initial condition. For $\mathcal{D} \neq 0$, information does propagate backwards, so the value of ρ and σ at the right boundary does matter, but we chose the space-time region in such a way that neither front ever came close to either boundary given the placement of the initial profile.

In order for this scheme to be stable, we require $\Delta t/\Delta x < 1$ for the case with $\mathcal{D} = 0$ or $\mathcal{D}\Delta t/(\Delta x)^2 < 1$ when $\mathcal{D}$ is finite (Courant condition, [29]). To ensure these criteria were met, we chose $\Delta t = \min\{0.25\ \Delta x, 0.25\ (\Delta x)^2/\mathcal{D}\}$. Instabilities were

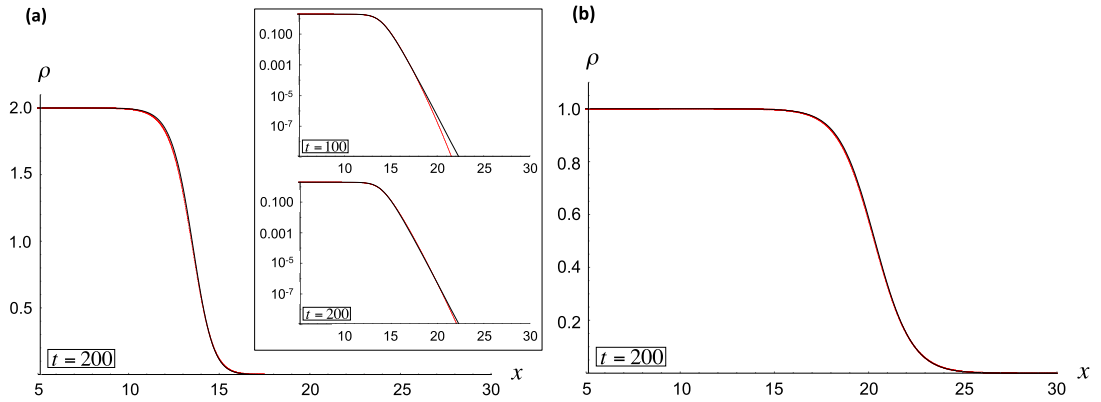

FIG. 18. Comparison of the heteroclinic solution of Eqs. (A1) and (A2)—UTF profile (thin black curve), with the numerical solution of the dimensionless version of Eqs. (1) and (2) of the main text (thick, red curve) at a given value of time, shifted to closely match the UTF profile [thus, the numerical values of the x axis do not correspond to the actual position of the front from the evaluation of Eqs. (1) and (2)]. (a) $a = 2, b = 1$. (b) $a = 0.1, b = 0.1$. The insets: time evolution, logarithmic scale.

never observed. Front speeds (and in some select cases, profile shapes) exhibited convergence when Δx was made progressively smaller. The results stated in Fig. 4 of the main text were obtained with $\Delta x = 0.025$ or a comparable value, which is $\ll$ physical characteristic length represented by $1/|\lambda_{\pm}|$ from Eq. (5) of the main text. The results stated in Fig. 3 were obtained with $\Delta x = 0.005$, with the exception for the upwind data in the left panel, where $\Delta x = 0.01$.

To find the speed of the wavefronts described by $\rho(x,t)$ and $\sigma(x,t)$, we tracked the position of the constant contour x_C, which is defined through $\rho(x_C,t) = C$ (Note, since ρ and σ have the same speed, we need only consider ρ or σ in our calculations). For example, to extract the speed of the downwind front, we used the following routine:

(1) At every time step t_n, find position of maximum $\rho(x,t)$, which we call $x_{\max}$.

(2) Extract all $\rho(x_m,t_n)$ to the right of this maximum: $\hat{\rho}(x_m,t_n) \equiv \rho(x_m > x_{\max},t_n)$. This function $\hat{\rho}$ is now unimodal.

(3) Then $x_C(t_n) = \min|\hat{\rho}(x,t_n) - C|$.

This results in a list $x_C(t_n)$, which after initial transients describes a straight line. The wave speed s is the slope of this line. We ran the calculations over a long time ($t = 800$ for the results stated in Fig. 4 of the main text) and discarded the first 50% of the data to remove transient behavior.

3. The role of numerical diffusion in long-time asymptotic solutions

It is known that our differencing scheme is also a lowest-order approximation to an equation with a small diffusion term, even if $\mathcal{D} = 0$ [29]. To underline the smallness of the role of any effective higher derivative terms on long-time asymptotic results, we show in Fig. 18 two plots of the profile shape for $\mathcal{D} = 0$ and compare them with the analytical front shape obtained from the UTF ansatz.

APPENDIX F: APPLICATION TO FUNGAL PATHOGEN TRANSPORT

This work was motivated by the problem of wind-driven transport of fungal pathogens on continental scales. Wind mediated fungal pathogen spread is a process involving production of spores, lifting, horizontal transport, and deposition [16–18,30,31].

In recent years, "reaction-dispersal" models [32] have been considered in the context of dispersal of biota, such as seeds and insects [33]. Such treatment describes random walks on multiple scales, and may be applicable over distances where the highly turbulent atmospheric boundary layer [34] (ABL)—the lowest level of the atmosphere—is the dominant mechanism of dispersal. However, the ABL tends to return the passive scalar back to the ground over the scale of its largest eddies, i.e., its own thickness of $O(1)$ km, so it is inefficient at much longer range transport. The Free Atmosphere (FA) located above the ABL emerges as a competing transport mechanism over longer length scales. The FA is less random than the ABL, contains persistent advective currents, and can carry passive scalar—including microorganisms—across continents [35] with characteristic speeds of $O(10)$ km/hr [36]. Reaction-dispersal models do not capture the role of the FA. We were motivated to (i) investigate the validity of ignoring advective transport channels that lie above the ABL and (ii) develop a theory of spatiotemporal dynamics of long-range biotic transport.

The main insight about the pathogen transport gained from our work is that the advective layer—such as the free atmosphere—cannot be ignored, even for very small rates of flow of mass into this advective layer. To make further statements, it helps to estimate our parameters a, b, and $\mathcal{D}$. We know that $a \ll 1$, because for a given amount of spores produced on the ground in a given time interval, most will return to the ground within 100 m [37], so only a very small fraction will leave the ABL, which has the width of the order of several kilometers [34]. The rate b is generally higher due to gravitational settling, but in the strong turbulence limit, both rates will be comparable (as in a pot on the boiler). To estimate the dimensionless diffusion $\mathcal{D}$, recall that it is given by $\frac{\delta D}{v_0^2}$. Here, v_0 is the speed of the free atmosphere, and it is of the order of 10 km/hr. We interpret D to be the eddy diffusion coefficient [38] of the small-scale turbulence that returns most particles to the ground within the aforementioned 100-m radius from the source. That is, this random transport is accommodated by much smaller eddies than those that

contribute to the interlayer transport. The eddy diffusion coefficient D is expected to scale as $\sim uL$, where u is the characteristic instantaneous velocity in the turbulence, and L is the scale of the eddy, i.e., 0.1 km in this case. For the speed scale we can use the friction velocity that determines the velocity scale in the surface-level turbulence, about 0.4 m/s [39]. So $D \sim O(10^{-1})$ km^2/hr.

Finally, we need a growth rate, δ. According to Ref. [40], a 5% disease severity amounts to 50 spore-producing postules per plant tiller. At this 5% disease severity, a plot will yield approximately two trillion spore/hectare/24-h [40], i.e., 2×10^8 spores per m^2 per day. If there are $O(100)$ plants per m^2 (for example, wheat plants), the production rate is 4×10^5 spores per postule per day. If each new spore were to lead to a fungus that produced only one postule, this would imply a multiplication rate of 4×10^5 spores per day produced from a single spore. In this paper, we assumed a logistic growth model, which reduces to exponential growth at low densities. Thus, an exponential growth model would thus give $4\times10^5 = e^{\delta\times 24\text{ hr}}$, giving $\delta \sim O(0.1)$ h^{-1}. All together, this gives $\mathcal{D} \sim O(10^{-4})$.

Evidently, the problem is completely dominated by the advection. Moreover, for parameters a and b both $\ll 1$, our theory predicts the speed is $\sim O$(advective speed), or propagation of a front by hundreds of kilometers per day. This suggests that this model is insufficient for the purpose of the application to fungal pathogen transport, because invasion fronts for observed pathogens, such as Wheat Stem Rust are expected to propagate tens of kilometers per day [18c]. Moreover, these numbers are based on the observations of incidences of disease symptoms on plants, not of spore densities. We are currently augmenting a model to include both the fungal density (immobile) and spore density (mobile), in addition to the effects of latency. Our current calculations show that spore death, for instance, a very well-known and important effect [18c], can decrease the front speeds dramatically. However, this discussion, in addition to the discussion of other biological specializations of the present theory will appear in a separate publication.

In the main text we argued that the mean-field description will hold when

$$\frac{a}{b} \gg \frac{\delta\lambda(a,b)}{\sigma_{\max} v_0}, \tag{F1}$$

where $\sigma_{\max}$ is the carrying capacity on the GL per unit length. In application of the fungal pathogen problem, the right-hand side of this equation is exceptionally small because of the largeness of the carrying capacity. We already know that $\lambda \to 1$ when $a,b \ll 1$. From the discussion above, we see that the order of magnitude of the carrying capacity will be billions of spores per m^2. Using 10^9 m$^{-2}\times 1$ m for $\sigma_{\max}$ (in our model, the densities are per length), we arrive at our estimate of 10^{-14} for the ratio of a/b above, which the mean-field model should hold. In other words, the mean-field theory is expected to hold if $a \gg 10^{-14}b$. Now, in the "pot on the boiler" limit when turbulence completely dominates vertical transport, we will have $a = b$, whereas in the limit of no turbulence (only gravitational settling), $a = 0$, while $b > 0$. We estimate roughly that $a/b \sim e^{-\frac{v_s}{v_T}}$, where v_s is the settling velocity ($\sim$0.01 m/s [40]) and v_T is velocity in the largest eddies that span the whole of the ABL (i.e., $\approx$1 km). It is known that the time scale for this large-scale turnover time is on the order of 1 h. Putting this together, we expect that $a/b \approx 0.97$. Thus, we are safely in the mean-field regime.

[1] R. Fisher, Ann. Eugenics **7**, 355 (1937).

[2] J. Murray, *Mathematical Biology. I: An Introduction* (Springer, New York, 2003).

[3] D. R. Nelson, Annu. Rev. Biophys. **41**, 371 (2012).

[4] A. Kolmogorov, N. Petrovsky, and N. Piskounov, Moscow Univ. Bull. Math. **1**, 1 (1937); J. F. Douglas, K. Efimenko, D. A. Fischer, F. R. Phelan, and J. Genzer, Proc. Natl. Acad. Sci. USA **104**, 10324 (2007); A. R. Kerstein, J. Stat. Phys. **45**, 921 (1986).

[5] S. N. Majumdar and P. L. Krapivsky, Physica A **318**, 161 (2003).

[6] B. Derrida and H. Spohn, J. Stat. Phys. **51**, 817 (1988); D. Carpentier and P. Le Doussal, Nucl. Phys. B **588**, 565 (2000).

[7] C. Marquet, R. Peschanski, and G. Soyez, Phys. Rev. D **73**, 114005 (2006); S. Munier and R. Peschanski, Phys. Rev. Lett. **91**, 232001 (2003); I. Balitsky, Nucl. Phys. B **463**, 99 (1996); Y. V. Kovchegov, Phys. Rev. D **60**, 034008 (1999); **61**, 074018 (2000); C. Marquet, R. Peschanski, and G. Soyez, Nucl. Phys. A **756**, 399 (2005).

[8] T. Chotibut, D. R. Nelson, and S. Succi, Physica A **465**, 500 (2017).

[9] G. Dumazer, M. Leda, B. Nowakowski, and A. Lemarchand, Phys. Rev. E **78**, 016309 (2008).

[10] J. R. H. Ross, *Heterogeneous Catalysis: Fundamentals and Applications* (Elsevier, Amsterdam, 2012).

[11] T. Gervais and K. F. Jensen, Chem. Eng. Sci. **61**, 1102 (2006).

[12] I. Blasco-Costa, J. M. Waters, and R. Poulin, Mol. Ecol. **21**, 207 (2012).

[13] E. Pachepsky, F. Lutscher, R. M. Nisbet, and M. A. Lewis, Theor. Pop. Biol. **67**, 61 (2005).

[14] R. Freter, H. Brickner, J. Fekete, M. M. Vickerman, and K. E. Carey, Infect. Immun. **39**, 686 (1983).

[15] J. Cremer, I. Segota, C. Yang, M. Arnoldini, J. T. Sauls, Z. Zhang, E. Gutierrez, A. Groisman, and T. Hwa, Proc. Natl. Acad. Sci. USA **113**, 11414 (2016).

[16] S. A. Isard and S. H. Gage, *Flow of Life in the Atmosphere: An Airscape Approach to Understanding Invasive Organisms* (Michigan State University Press, East Lansing, 2001).

[17] R. Nathan, G. G. Katul, H. S. Horn, S. M. Thomas, R. Oren, R. Avissar, S. W. Pacala, and S. A. Levin, Nature **418**, 409 (2002).

[18] D. E. Aylor, Ecology **84**, 1989 (2003); S. A. Isard, S. H. Gage, P. Comtois, and J. M. Russo, BioScience **55**, 851 (2005); D. E. Aylor, Agric. Forest Meteorol. **38**, 263 (1986).

[19] W. van Saarloos, Phys. Rep. **386**, 29 (2003).

[20] We also tested Gaussian ICs with width $\gg$ spatial grid spacing, for select parameters. The profile speed and the front shape approached the point IC results as time progresses.

[21] M. A. Lewis and G. Schmitz, Forma **11**, 1 (1996).

[22] We slightly overloaded the notation: now $(\lambda_\pm^*, s_\pm^*)$ represents extremum points of $s(\lambda)$ and selected downwind and upwind

fronts from a δ-function IC. However, they are expected to be the same [19].

[23] C. M. Bender and S. A. Orszag, *Advanced Mathematical Methods for Scientists and Engineers* (McGraw-Hill, New York, 1978).

[24] If $\mathcal{D} \to 0$ by letting $\delta \to 0$, then $a,b \to \infty$, so $s_+^*(\mathcal{D}=0) \to (1+b/a)^{-1} > 0$.

[25] We note that although $a\rho = b\sigma$ for all x only when $\mathcal{D} = 1/4$, this equality of currents is still true for other $\mathcal{D}$ wherever ρ and σ are constant, i.e., far away from any fronts.

[26] V. Méndez, S. Fedotov, and W. Horsthemke, *Reaction-Transport Systems: Mesoscopic Foundations, Fronts, and Spatial Instabilities* (Springer-Verlag, Heidelberg, 2010).

[27] Since $b = 0$ is a singular limit, one has to exercise caution. At $a = 1$, the limit $b \to 0$ of the right-hand side of Eq. (A6) reads

$$\frac{1}{2\lambda^2}\left[\frac{\mathcal{D}\lambda(\sqrt{\lambda^2(\mathcal{D}\lambda-1)^2}+\lambda(\mathcal{D}\lambda-1))}{\mathcal{D}\lambda-1}\right].$$

The (positive) quantity $\sqrt{\lambda^2(\mathcal{D}\lambda-1)^2} = \lambda(\mathcal{D}\lambda-1)$ for $\lambda < 0$ and for $\lambda > 1/\mathcal{D}$. Otherwise, $\sqrt{\lambda^2(\mathcal{D}\lambda-1)^2} = -\lambda(\mathcal{D}\lambda-1)$ to ensure positivity. This choice implies that $ds_1/d\lambda = \mathcal{D}$ for $\lambda < 0$ and for $\lambda > 1/\mathcal{D}$, while it is 0 otherwise. We could follow a similar argument for $s_1(\lambda)$ and $s_2(\lambda)$ directly and reach the same conclusion about their piece-wise nature. Note that setting $b = 0$ *a priori* in Eq. (A3) [it would have to be multiplied out by $b + (s-1)\lambda$ first] would give 1 and $\mathcal{D}\lambda$ as the two branches of $s(\lambda)$ for $\lambda \neq 0$ (and at $a = 1$). This discrepancy is the manifestation of $b = 0$ being a singular limit. Similar remarks apply to the $b \to 0$ limit at other fixed a, the $a \to 0$ limit at fixed b, and to the $a \to 0, b \to 0$ limit. Finally, when Taylor expanding the right-hand side of Eq. (A6) in b, the quantity $\sqrt{\lambda^2(\mathcal{D}\lambda-1)^2}$ will also make an appearance, which we must treat similarly to describe the correct branches at finite b.

[28] P. R. Garabedian, *Partial Differential Equations* (Wiley, New York, 1964); J. Ockendon, S. Howison, A. Lacey, and A. Movchan, *Applied Partial Differential Equations*, rev. ed. (Oxford University Press, Oxford, 2003).

[29] W. H. Press, S. A. Teukolsky, W. T. Vetterling, and B. P. Flannery, *Numerical Recipes: The Art of Scientific Computing,* 3rd ed. (Cambridge University Press, Cambridge, 2007).

[30] A. Sesartic and T. N. Dallafior, Biogeosciences **8**, 1181 (2011), and references therein.

[31] G. N. Agrios, *Plant Pathology*, 5th ed. (Elsevier Academic Press, Amsterdam, Boston, 2005); L. V. Madden, G. Hughes, and F. van den Bosch, *The Study of Plant Disease Epidemics* (American Phytopathological Society Press, St. Paul, 2007).

[32] O. Hallatschek and D. S. Fisher, Proc. Natl. Acad. Sci. USA **111**, E4911 (2014).

[33] S. Thompson and G. Katul, Am. Nat. **171**, 468 (2008); M. Kot, M. A. Lewis, and P. van den Driessche, Ecology **77**, 2027 (1996); for a review of seed dispersal models, see S. A. Levin, H. C. Muller-Landau, R. Nathan, and J. Chave, Annu. Rev. Ecol. Evol. Syst. **34**, 575 (2003).

[34] J. R. Garratt, *The Atmospheric Boundary Layer* (Cambridge University Press, Cambridge, 1992).

[35] D. Jaffe, T. Anderson, D. Covert, R. Kotchenruther, B. Trost, J. Danielson, W. Simpson, T. Berntsen, S. Karlsdottir, D. Blake, J. Harris, G. Carmichael, and I. Uno, Geophys. Res. Lett. **26**, 711 (1999); J. M. Prospero and T. N. Carlson, J. Geophys. Res. **77**, 5255 (1972); J. M. Prospero, E. Blades, G. Mathison, and R. Naidu, Aerobiologia **21**, 1 (2005); J. M. Prospero, Proc. Natl. Acad. Sci. USA **96**, 3396 (1999).

[36] J. Pedlosky, *Geophysical Fluid Dynamics*, 2nd ed. (Springer-Verlag, New York, 1987).

[37] A. P. Roelfs, Phytopathology **62**, 70 (1972).

[38] H. Tennekes and J. L. Lumley, *A First Course in Turbulence* (MIT Press, Cambridge, 1972).

[39] M. Chamecki and C. Meneveau, J. Fluid Mech. **683**, 1 (2011).

[40] A. P. Roelfs, Epidemiology in North America, in *The Cereal Rusts, Volume II: Diseases, Distribution, Epidemiology, and Control*, edited by A. P. Roelfs and W. R. Bushnell (Academic Press, Orlando, 1985).